Homogeneous Supported Monolayer from Microbial Glycolipid Biosurfactant

Niki Baccile, Anyssa Derj, Cedric Boissiere, Vincent Humblot, Ariane Deniset-Besseau

Homogeneous Supported Monolayer from Microbial Glycolipid Biosurfactant

Niki Baccile,[a,*] Anyssa Derj,[a] Cédric Boissière,[a] Vincent Humblot,[b,c] Ariane Deniset-Besseau[d]

[a] Sorbonne Université, Centre National de la Recherche Scientifique, Laboratoire de Chimie de la Matière Condensée de Paris, LCMCP, F-75005 Paris, France

[b] Sorbonne Université, Laboratoire de Réactivité de Surface (LRS), UMR CNRS 7197, 4 place Jussieu, Paris, F-75005, France

[c] Current address : FEMTO-ST Institute, UMR CNRS 6174, Université Bourgogne Franche-Comté, 15B avenue des Montboucons, 25030 Besançon Cedex, France

[d] Université Paris-Saclay, CNRS, Institut de Chimie Physique, UMR 8000, 91405, Orsay, France

* Corresponding author:
Dr. Niki Baccile
E-mail address: niki.baccile@sorbonne-universite.fr
Phone: +33 1 44 27 56 77

Abstract

The development of supported glycosylated lipid layers is an important trend in the field of glyconanomaterials for their interest in understanding sugar-sugar and protein-sugar interactions, these being at the core of cellular, bacterial or viral adhesion. The conventional self-assembled monolayer (SAM) approach generally requires a thiolated glycoconjugate and a gold substrate. In this work, we show how glycolipid amphiphiles of natural origin, commonly known as microbial biosurfactants, can be easily deposited onto a substrate. Spontaneously produced by microorganisms but lacking a thiol group, one can take advantage of their self-assembly properties to prepare homogeneous supported lipid monolayers (SLM). We then choose a saturated glucolipid, G-C18:0, which forms a colloidal lamellar phase under diluted conditions. The lamellae can then be deposited onto a substrate (silicon, gold) using a physical method (dip coating). Dip coating is preferred over more classical deposition methods (Langmuir-Blodgett-LB-, vesicle fusion or spin-coating) because of its versatility, compatibility with aqueous solutions and robust control of the thickness below 10 nm. Defect-free glycosylated SLM from a microbial biosurfactant are then easily developed. A combination of ellipsometry, fluorescence microscopy, atomic force microscopy and infrared nanospectroscopy (AFMIR) show that the glycosylated SLM are defect-free, have a thickness of 2.8 ± 1.0 nm and they are highly homogeneous at scales going from the *nm* to *cm*.

Keywords: supported lipid bilayers; microbial glycolipids; microbial biosurfactants; dip-coating

Introduction

Glycoconjugates constitute a broad family of sugar-based lipids, which combine chemical functionality, lipid self-assembly and the properties of carbohydrates.[1] Association of glycoconjugates to nanoscience contributed to develop the field of multidimensional glyconanomaterials like vesicles,[2] nanoparticles[3] or functional surfaces.[4] Interesting for their hydration,[5] interactions against lectins[6–8] or between carbohydrates themselves,[9] two-dimensional, supported, glyconanomaterials have found a specific interest for their tunable adhesive,[4] anti-adhesive[1,10] and antimicrobial properties[11,12] but also to better understand virus binding mechanisms.[13] Glycosylated surfaces are generally prepared by a classical self-assembled monolayer (SAM) process, involving chemisorption of thiolated glycoconjugates onto gold.[3,4,10,11] However, this approach naturally requires the use of a gold support and tailor-made glycoconjugates, of which the synthesis, involving tedious multiple chemical steps typical

2

in the chemistry of sugars, is cumbersome and of which the complexity may prevent transferring the applications to larger scales and into devices. It could then be attractive to prepare glycosylated monolayers from ready-made glycoconjugates.

Microbial amphiphiles, known as biosurfactants, are produced by the fermentation of specific yeasts, or bacteria, in the presence of fatty acids and glucose.[14,15] Natural glycoconjugates due the presence of a freely accessible COOH group, microbial biosurfactants constitute an interesting biobased source to prepare 2D glyconanomaterials. However, unless specifically modified, as previously done for sophorolipids,[11,12,16] microbial biosurfactants do not have a thiol group, making the formation of SAM quite difficult. Worst, not all biosurfactants (e.g., surfactin) have a chemically-active group in their molecular structure, thus making derivatization of a thiol conjugate a harsh task of its own. However, their rich phase behaviour in bulk water,[17–22] combined with a physical deposition method, could be exploited to prepare 2D glyconanomaterials in the form of supported lipid bilayers (SLB).

Since the work of Tamm,[23] SLB have generated a wide interest across disciplines. Initially proposed as model systems to understand the behavior of biological lipid membranes[24–26] and their interactions with proteins and surfactants,[27,28] they have recently stimulated new branches of research in materials' science.[26,29] In the field of nanotechnology for instance, it was shown that SLB are interesting supports to control the epitaxial growth in inorganic nanomembranes, like ZnO,[30] while in the field of biomedical engineering, they are highly-demanded microscale environments for cell adhesion, proliferation, and differentiation.[31–33] SLB are also highly demanded to understand the interactions between nanocolloids like particles[34] or viruses[13,35] and model lipid membranes.

Preparation of SLB by mean of well-established physical methods does not require the use of functional lipids and the variety of supports is broader. Langmuir-Blodgett (LB)[23,24,36] and vesicle fusion[25,37–43] are by far the most recurrent ones but other methods like drop casting,[44] spin coating[45–50] or knife coating[51] have been developed in the past two decades. Unfortunately, some of these methods are not easy to setup and in many cases achieving large-scale homogeneity of the thickness using physical methods is not guaranteed. Most of them require solubilization of the lipid in a solvent (vesicle fusion, spin coating or knife coating), the use of a specific apparatus (Langmuir trough in LB) or provide multilamellar thick films (drop casting). When the physical properties (e.g., melting temperature, phase diagram, solubility) of the lipid are well-known, as for many phospholipids, LB and vesicle fusion can provide good quality SLB,[24] but in most cases, solvent evaporation (vesicle fusion) or strong mechanical solicitations (spin coating), generate cracks and poor homogeneity.[24,25,50,36,38,41,42,46–49]

Since neither the physical nor the interface properties of microbial biosurfactants are as well known as for phospholipids,[52] most of the physical methods above could generate inhomogeneous SLB. For this reason, we employ dip coating, an evaporation-induced process generally employed in the synthesis of inorganic coatings,[54] but having multiple advantages over the above-mentioned conventional methods: 1) it can be used with both aqueous solutions and colloidal dispersions; 2) coating thickness and homogeneity can be tuned during the dipping process through the dipping rate, humidity and temperature; 3) it was shown to form sub-10 nm coatings.[54]

Previously adopted to deposit another well-known biosurfactant, sophropolipids, onto gold, silicon and titania substrates,[53] we found that coatings were structured but still poorly homogeneous. That finding was attributed to the impact of surface energy to the surface assembly of sophorolipids. For this reason, we employ here another microbial glycolipid amphiphile, the acidic C18:0 glucolipid biosurfactant (G-C18:0, Figure 1a), derived from the fermentation of the yeast *S. bombicola ΔugtB1*.[55] G-C18:0 is more atypical than sophorolipids, as in the neutral-acidic pH range, it forms a stable colloidal dispersion of flat lamellae in water (Figure 1b), instead of micelles.[20,21] Our strategy then consists in dipping a given substrate (silicon or gold) into a colloidal solution of pre-formed lipid lamellae.

A combination of ellipsometry, optical microscopy, atomic force microscopy (AFM) and infrared nanospectroscopy (AFMIR) shows that a colloidal dispersion of lamellae composed of G-C18:0 can be deposited onto a silicon and gold substrate. The supported 2D glyconanomaterial has a sub-10 nm thickness and homogeneity from the *nm*- to the *cm*-scale in the substrate plane. Considering the relatively poor knowledge concerning the behavior of microbial biosurfactants are solid-air interfaces,[52] this work could certainly open new perspectives for this class of amphiphiles.
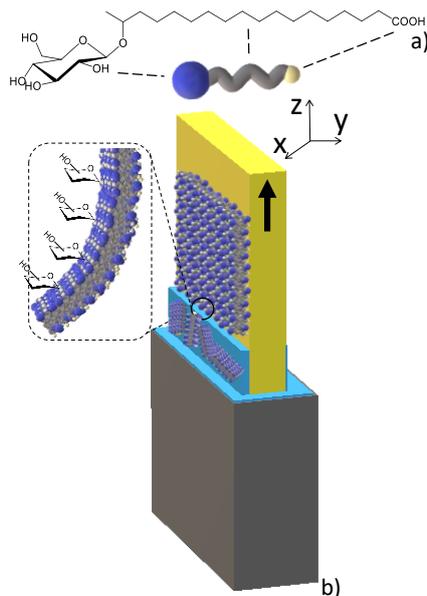
Figure 1 – a) Chemical structure of the microbial glucolipid G-C18:0, Schematic representation of G-C18:0, blue sphere: glucose, grey tail: C18:0 chain, yellow sphere, COOH. b) Scheme of the dip-coating process employed to prepare glycosylated SLM from an aqueous colloidal dispersion of self-assembled interdigitated G-C18:0 lamellae at C< 1 wt%.

Experimental section

The experimental section is given in the Supporting Information.

Results and discussion

G-C18:0 microbial glucolipids (Figure 1a) are insoluble in water below pH 7, when they self-assemble into a lamellar phase between 0.1 wt% and 10 wt%.[20,21,56,57] At concentrations below 1 wt%, the corresponding aqueous solution is composed of colloidally-stable infinitely flat membranes, of thickness about 3.6 nm, as determined by cryo-TEM and small angle X-ray scattering.[20,21] The thickness corresponds to the typical length of a single G-C18:0 molecule, thus suggesting that the lamellae are interdigitated monolayers, as sketched in Figure 1b. This is not unexpected, because G-C18:0 has a bolaform shape and interdigitation in bolaform monolayer membranes was addressed before.[58] Even if the monolayer organization of G-C18:0 membranes could recall the structure of SAM, the method to prepare coatings from G-C18:0 membranes and the lack of specific interactions with the support (e.g., thiol-gold, as found in SAM) makes this work conceptually closer to the field of SLB. In the following, we will then use the acronym SLB, when referring to specific literature studies in this field, and the acronym SLM, when referring to the synthesis of supported lipid monolayers prepared from the

microbial G-C18:0 glucolipid throughout the present study.

If any of the classical methods employed to prepare SLB could be employed, none of them is ideal to prepare SLM from G-C18:0. The conditions to form a self-assembled G-C18:0 monolayer at the air-water interface were never studied and its solubility was never studied either, thus making the LB and spin coating approaches not straightforward. In a previous study, we have observed that G-C18:0 can partially form vesicles above 70°C, but, first of all, this observation was not quantitative, and, secondly, controlling the conditions for a homogeneous coating at such temperature can be challenging. For this reason, the vesicle fusion approach to prepare SLM is poorly advisable here. Finally, the drop-casting could be an interesting method and it was used before on this systems to measure short-range hydration forces,[59] but only multilamellar coatings were obtained. For these reasons, we employ an evaporation induced coating method employed here in a vertical dip-coating geometry, never reported before within the frame of SLB.

The use of dip-coating under controlled conditions of temperature, relative humidity and withdrawal rate is fully justified by the possibility to deposit a homogeneous coating using aqueous solution on either Si wafers or Au substrates, both being poorly wet by water (contact angle is $69° \pm 4°$ for Au and $43° \pm 4°$ for Si).[53] The dip-coating apparatus employed in this work allows controlling the humidity and temperature in the dip-coating chamber as well as the dip coating rate between 10^{-3} and 10 mm/s. This was demonstrated to be a range broad enough to span from the capillarity to the draining regimes, providing highly homogeneous thin films with thickness, T_h, varying from 10 to 10^3 nm.[54] T_h is measured with ellipsometry, a fast-screening, mm-scale, probe with Å-resolution even below 10 nm, if the boundaries of the refractive index are defined with caution (please refer to the Supporting Information for a detailed discussion on the fitting strategy).[39] A description of the technique, as well as the models and strategy chosen in this work to fit the amplitude $\Psi(\lambda)$ and phase difference $\Delta(\lambda)$ and to extract the sample thickness and refractive index (RI), are described in more detail on P. S3-S5 in the Supporting Information with reference to Figure S 2a, Table S 1 (for Si wafer) and Figure S 3a, Table S 2 (for Au substrates) in the same document.

Two glucolipid G-C18:0 solutions at pH of 9 and 6 are deposited by dip-coating on silicon wafers, employing the dip-coating apparatus described in Figure S 1. This apparatus is developed for the deposition of high-quality thin films with control of temperature, T, and relative humidity, RH%. The entire set of data collected throughout this study is provided in Table S 3, of which a reasoned overview is given in Figure 2 and Figure S 4, discussed hereafter. To prove the formation of a SLM, one should only consider measured thickness values between

2 nm and 10 nm within the frame of the Cauchy fitting model, whereas optimum values are expected to be between 3 nm and 5 nm. It was previously shown that withdrawal rate has a huge impact on the film thickness in water,[54] and for this reason this is the first parameter tested here.

Figure 2a and Figure 2c show the evolution of the lipid film thickness as a function of the dip-coating rate, varied between 0.02 and 10 mm/s. The minimum, around 3 nm, and the maximum, around 100 nm, thickness values are systematically recorded, respectively, around S_w of 0.1 mm/s and 10 mm/s, independently from the pH value, temperature or relative humidity. This is in good agreement with the data reported for inorganic oxides, for which it was shown that the smallest thickness is generally obtained with S_w in the order of 0.1 mm/s. In the water on silicon system, the rate of 0.1 mm/s corresponds to the interval between the low-speed, capillary, and high-speed, draining, regimes, where thickness is minimized.[54] All samples prepared at low S_w are of good quality (red circles in Figure 2a,c) and display a homogeneous thickness on at least 5% of the coated surface. This is estimated by combining the quality of the fit (for a typical good quality fit please refer to Figure S 2b) and the surface probed by the beam (beam size is between 0.15 cm^2 and 0.20 cm^2, to be compared with a coating of about 3 cm^2). Selected samples have been analyzed on three different spots without any obvious change in the $\Psi(\lambda)$ and $\Delta(\lambda)$ spectra, thus indicating a homogeneity on at least 15% of the total surface, suggesting a *cm*-scale homogeneity of the coating. At higher S_w, the samples are thicker and inhomogeneous, and of overall poorer quality, as indicated by the green and blue colored circles in Figure 2a,c. In the following, we will only discuss the most homogeneous samples obtained with $0.055 < S_w / \text{mm/s} < 0.2$.
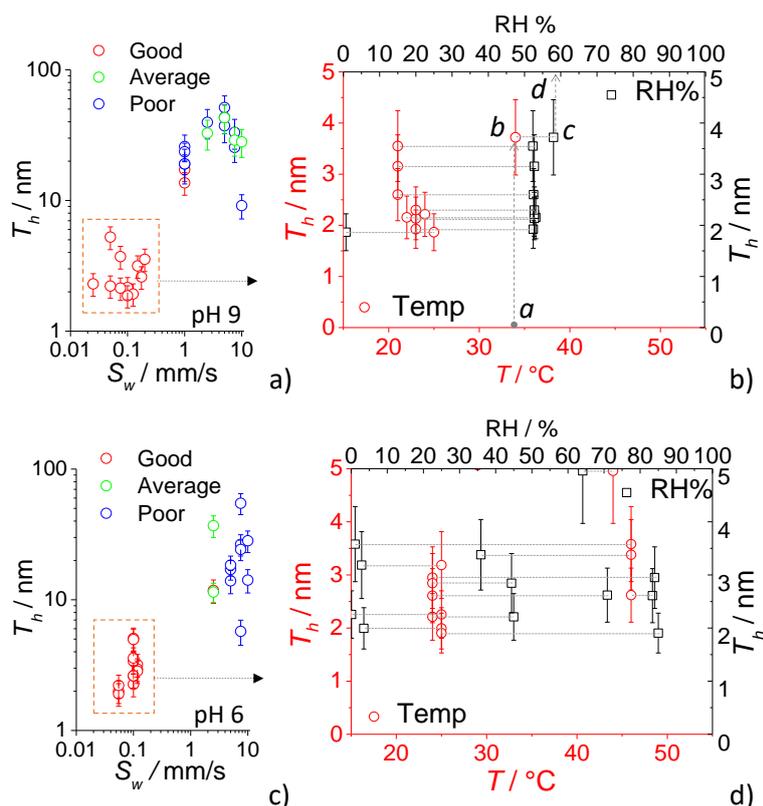
Figure 2 – Thickness, T_h, of the dip-coated G-C18:0 lipid film measured by ellipsometry as a function of temperature, T, withdrawal rate, S_w, and relative humidity, $RH\%$ and prepared from a lipid solution at $C_{\text{G-C18:0}}$= 5 mg/mL. a,c) Evolution of T_h as a function of S_w for lipid solutions prepared at (a) pH 9 (red samples in Table S 3) and (c) pH 6 (green samples in Table S 3) for a wide range of T (23°C – 50°C) and $RH\%$ (5% - 90%). b-d) Evolution of T_h as a function of $RH\%$ and T for lipid solutions prepared at (b) pH= 9 and (d) pH 6 for S_w= 0.13 ± 0.10 mm/s. In graphs (b) and (d), T_h given by red circles (left ordinate, bottom T abscissa) is correlated to T_h values given by black squares (right ordinate, top $RH\%$ abscissa) through the dotted grey line. For a given T (e. g., point a on the bottom red abscissa, graph in b)), one reads the corresponding T_h (red circle b, left red ordinate). Following the horizontal grey line leads to point c (black square, right ordinate), of which the corresponding $RH\%$ is given by the top black abscissa (point d).

The second parameter of major importance is the lipid concentration in the parent solution. Figure S 4a shows the evolution of T_h at three lipid concentrations (1, 3 and 5 mg/mL) in the parent solution at pH 6. All corresponding $\Psi(\lambda)$ and $\Delta(\lambda)$ spectra can be satisfactorily fitted (Table S 3) and one finds that concentrations below 5 mg/mL, independently from the temperature and relative humidity, provide lipid coatings of thickness being significantly less than 2 nm, which is not a physically-acceptable result. This could either indicate that the coating does not take place or, most likely, the presence of an inhomogeneous coating. For this reason, most data presented hereafter will mainly concern lipid solutions at concentration of 5 mg/mL, both at acidic and basic pH.

Relative humidity and temperature are two important parameters, which are known to have a strong impact on the thickness of thin solid films.[54] Figure S 4b shows the evolution of T_h as a function of $RH\%$ for samples prepared from acidic and basic solutions at C= 5 mg/mL, several withdrawal rates contained in the range, S_w= 0.13 ± 0.10 mm/s and a range of temperature between 25°C and 50°C. At acidic pH (red circles), the thickness is systematically between 2 nm and 5 nm, independently from the value of $RH\%$. At basic pH, on the contrary, only samples in the range $40 < RH\% < 70$ show thickness between 2 nm ad 5 nm, while $T_h \leq 2$ nm for higher and lower $RH\%$. To understand whether or not temperature plays a role, a more precise correlation between $RH\%$ and T is shown on Figure 2b and Figure 2d (refer to legend of Figure 2b,d for more details in the graph readability) only for those samples in Figure S 4b having a physically real thickness above 2 nm. At both basic and acidic pH, the values of T_h is always contained between 2 nm and 5 nm in the range of temperature explored (25°C - 45°C), without any specific trend between room temperature and 45°C.

In summary, ellipsometry experiments indicate that dipping a solution of G-C18:0 glucolipid (C= 5 mg/mL) on a Si wafer provides homogeneous SLM on the *cm*-scale and of average thickness, T_h= 2.8 ± 1.0 nm. This result is quite robust, because the error, less than 50%, is calculated over 26 experiments (Figure 2b,d) performed within a broad range of dipping parameters (S_w= 0.13 ± 0.10 mm/s, T= 30 ± 10°C and $RH\%$= 55 ± 10%). If these conditions hold for glucolipid solutions at acidic and basic pH, the impact of relative humidity at acidic pH seems much more limited, and good quality coating can be obtained in a humidity range between 5% and 90%. These conditions are also summarized in Table 1, which in fact provides a broader confidence rage of thickness (2 nm – 10 nm). This is meant to remind the uncertainty associated to the Cauchy model employed to fit of $\Psi(\lambda)$ and $\Delta(\lambda)$ profiles. This model provides a good description for those samples prepared under the conditions depicted in Table 1 but it probably fails for those experimental conditions providing coating of $T_h < 2$ nm. For this reason, ellipsometry measurements should be coupled to more local probes, which can give a better insight of the coating's homogeneity, composition and possibly thickness at the *mm-* and *μm-*scales.

Table 1 – Most suitable experimental conditions to prepare homogeneous G-C18:0 SLM between $2 < T_h$ / nm < 10 using a Si wafer substrate estimated by ellipsometry experiments.

pH of solution	Concentration of solution / mg/mL	Range of T_h / nm	Range of T / °C	Range of $RH\%$
6	5	2 – 15	20 - 45	5 – 90
9	5	2 – 15	20 - 40	40 - 70

Optical fluorescence microscopy has long been used to study the homogeneity[60] of SLB on the *mm*-scale as well as their dynamic properties through fluorescence recovery after photobleaching (FRAP).[29,60,61] Fluorescence microscopy is recorded on two sets of samples, at high and low S_w. Figure 3a,b shows the typical images of two heterogeneous coatings prepared at S_w= 5 mm/s at both acidic and basic pH, in agreement with the corresponding ellipsometry data (blue circles in Figure 2a,c). According to ellipsometry, these samples have an average thickness between 10 nm and 50 nm, which could explain the heterogeneous fluorescence signal. On the contrary, Figure 3c,d show two samples prepared from both acidic and basic solutions at S_w= 0.1 mm/s. In this case, fluorescence microscopy shows a homogeneous image with a poorly contrasted fluorescence signal, making it nearly impossible to determine the presence of the fluorophore and its distribution across the sample. If these images are in agreement with a *mm*-scale homogeneous distribution of the fluorophore within a sub-10 nm coating, standard and spectroscopic AFM are performed on selected samples prepared at S_w= 0.1 mm/s to confirm the coating homogeneity and its composition.
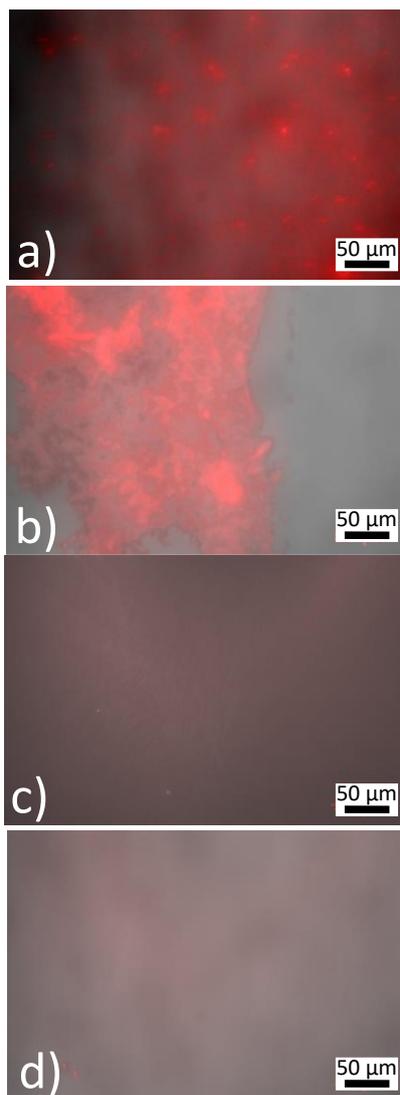
Figure 3 – Fluorescence microscopy experiments performed on G-C18:0 lipid coated silicon substrates. Lipid solutions contain *Liss* in 200:1 lipid:*Liss* molar ratio. a) Sample 187 (pH 9) and b) sample 203 (pH 6) are dip-coated at the unfavorable conditions of S_w= 5 mm/s, while c) sample 171 and d) sample 173 are dip-coated at the favorable conditions of S_w= 0.1 mm/s. Sample list is given in Table S 3.

Figure 4 presents the AFM images, and their corresponding height, *h*, profiles, recorded on silicon substrates coated from acidic (a,b) and basic (c,d) lipid solutions. Disregarding some typical artifacts like surface contamination (SC) or line streaks (LS),[62] Figure 4a,c, recorded on 50 x 50 μm and 20 x 20 μm surface areas, show a thoroughly homogeneous surface, closely looking like the control, undipped, silicon substrate (Figure S 5, also containing SC and LS artifacts). No clearly identified edges, multilayers or holes can be observed, as commonly found in classical AFM imaging of SLB.[27,36,47,63–66] The homogeneity of the samples in Figure 4 compared to the Si wafer control is also demonstrated by the surface roughness (*R*) parameters, all shown in Table S 4 and related description in the Supporting Information. The height profile

of the control is given as a reference in Figure S 5a but also superimposed as a red line to the $h(d)$ profiles below Figure 4a,c.
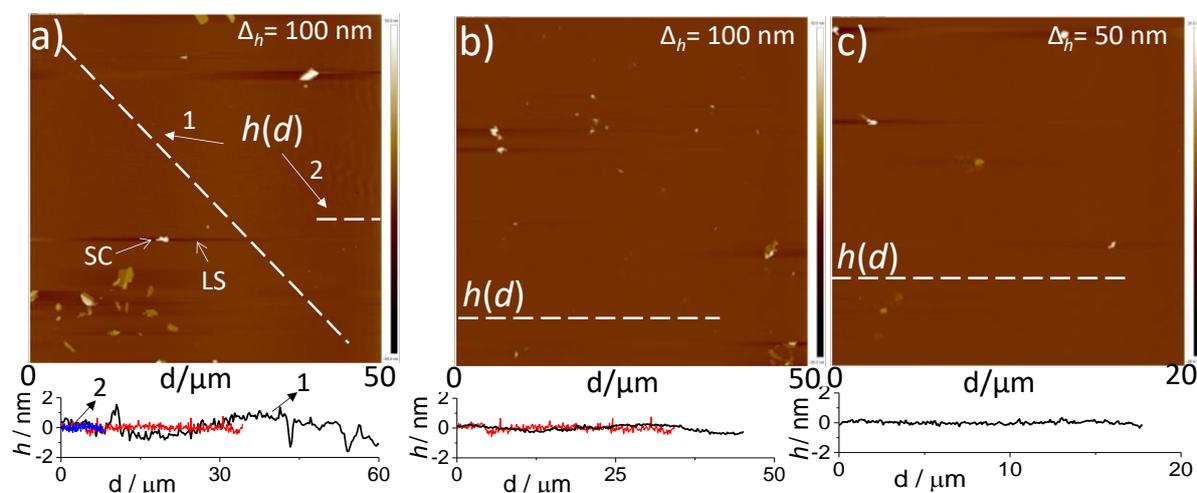

Figure 4 – AFM experiments performed on G-C18:0 lipid coated Si wafer substrates (S_w= 0.1 mm/s and $RH\%$= 66%). a) Sample 171; b,c) Sample 176. Sample list is given in Table S 3. Height acronyms: Δ_h= peak-to-valley thickness on the entire image; $h(d)$= thickness *vs*. distance profiles are represented by the segmented white line and correspondingly given below each image (black). The red profile in a) and b) corresponds to the bare, control, silicon substrate, shown in Figure S 5a. Artifact acronyms: LS= line streaks; SC= surface contamination.

The surface roughness analysis shows that: 1) the roughness is less than 1 nm on distances between 15 and 60 μm, that is an approximate scale ratio of 1:10⁵; 2) the roughness in the samples is comparable to the bare silicon wafer. These points quantify the *μm*-scale homogeneity of the G-C18:0 lipid coating onto silicon on selected samples of T_h< 10 nm; however, they also raise a fundamental question about the actual surface coverage. To prove the presence of single, or even multi, lipid layer(s), AFM requires a clear-cut difference in height between the coating and the substrate. In the case of a thoroughly homogeneous coverage, as shown in Figure 4, it is virtually impossible to confirm the presence of a lipid layer onto the substrate. In addition, all tentative AFM imaging performed on the most homogeneous samples, selected according to ellipsometry and fluorescence microscopy, provide similar images to what we show on Figure 4. Surface scratching is sometimes used as a way to remove the coating to measure its thickness with respect to the scratched background; however, in the case of SLB, it was shown that this approach is not reliable: lipids can be pushed towards the surface, instead of being removed, they can adsorb onto the tip or they can also diffuse back to fill up the hole soon after scratching.[65–67] To study the coating homogeneity and its composition

at the same time, we then perform additional spectroscopic experiments combining AFM and infrared spectroscopy.

IR spectroscopy associated to AFM (AFMIR) is a recently-developed technique[68] allowing local infrared analysis with sub-wavelength spatial resolution[69,70] and employed for chemical mapping at the nanoscale on a wide range of inorganic, organic and biological systems.[71–74] In this study, AFMIR experiments are performed on a series of G-C18:0 lipid coated gold substrates, the latter, associated to gold-coated tip, ensuring an enhancement of the local electric field, thus improving the sensitivity of the technique. If the use of gold instead of silicon could induce changes in the surface aggregation of other glycolipids, like sophorolipids,[53] we exclude major effects, as shown in the Supporting Information (discussion on Page S16-17 in relationship with Figure S 6 and Table S 5 in the same document). Under similar dipping conditions, the use of a gold substrate promote an equally homogenous, although slightly thicker (by a factor about two), lipid coating.

[1]: 1720-1740 cm⁻¹ – ν(COOH) [isolated]
[2]: 1700-1720 cm⁻¹ – ν(COOH) [H-bonding]
[3]: 1650 – 1660 cm⁻¹ - ν(H₂O) [adsorbed]
[4]: 1580 cm⁻¹ - ν$_{as}$(COO⁻)
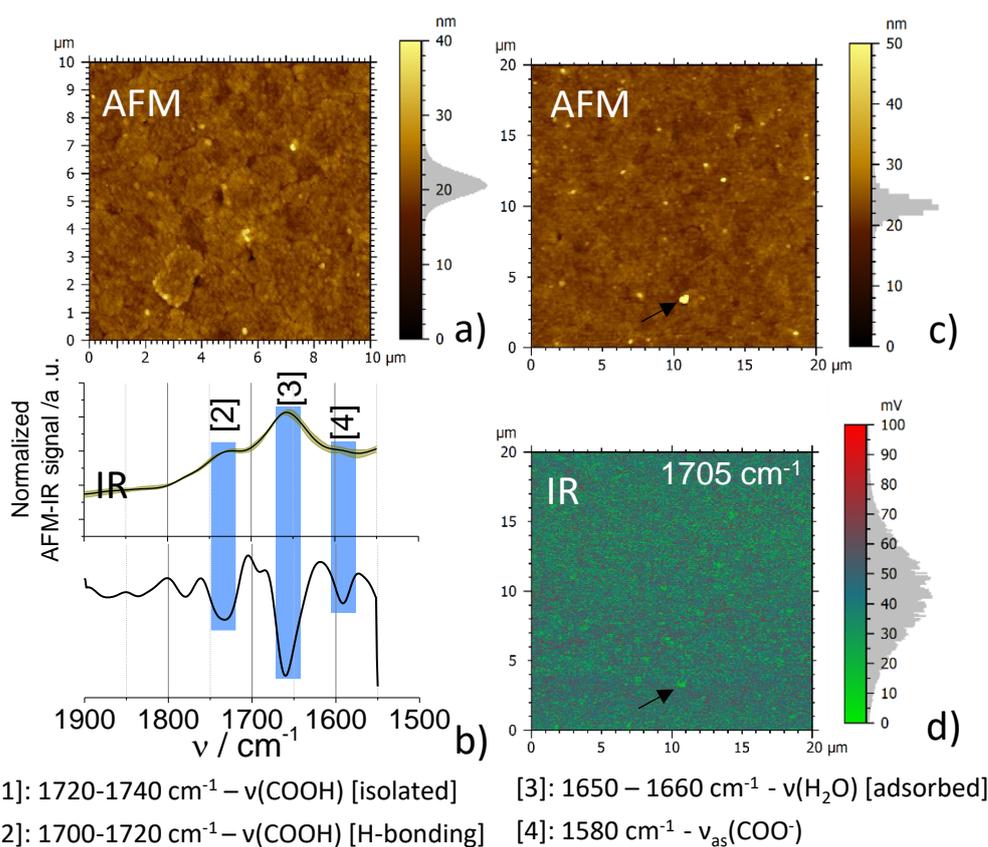
Figure 5 – AFMIR experiments performed on G-C18:0 lipid-coated gold substrates (Sample N°175, Table S 3.) dipped at the optimal conditions of S_w= 0.1 mm/s. a) 10x10 μm AFM image and corresponding b) normalized IR absorption spectrum with second derivative given underneath. The background signal (Figure S 5d, average over 15 spectra), measured on a lipid-free gold substrate (Figure S 5b,c), is subtracted from the IR spectrum, which results from the average of 40 spectra, randomly collected on the AFM image in a). The shaded region surrounding the spectrum corresponds to the intensity dispersion evaluated form

Figure 5 and Figure 6 present a series of AFMIR experiments performed at different scales, from 50 µm x 50 µm to 10 µm x 10 µm, on several G-C18:0 coated gold substrates. All AFM images in Figure 5 and Figure 6, in agreement with the AFM experiments performed on Si wafers (Figure 4), show a homogeneous surface coverage, irrespective of the sample under study and of the region of the substrate, without any irregularity or defect in the coating. The faceted surface texture observed for all samples is not related to the lipid coating but it is typical of these substrates, as shown on AFM image of the lipid-free, control, Au substrate (Figure S 5b,c).

The normalized IR spectra (non-normalized spectra are shown in Figure S 7) and related second derivatives are shown below each AFM image for a given sample in Figure 5 and Figure 6. Due to spectral range of the IR laser source limited to 1945-1510 cm^{-1}, AFMIR covers the $1900 < v\ /\ \mathrm{cm}^{-1} < 1500$ region, which corresponds to the v(C=O) in COOH and $v_{s,as}$(C=O) in COO^{-},[75] that is the carboxylic/carboxylate region, typical of G-C18:0 and microbial glycolipids[76] and excluded in surface organic impurities, generally characterized by the $v_{s,as}$ CH signal above 2000 cm^{-1}. The COOH group has a typical signature between 1760 cm^{-1} and 1700 cm^{-1}, depending on the strength of hydrogen bonding,[75] while COO^{-} has two typical signatures, reported for organic acids at v_{as}(COO^{-})= 1579 ± 26 cm^{-1} and v_{s}(COO^{-})= 1406 ± 12 cm^{-1},[75] the latter being out of the spectral window in this work. In this regard, AFMIR confirms that the uncoated gold substrate control does not show any spurious signal below 2000 cm^{-1} (Figure S 5d), that is in the range of the C=O stretch.

IR data associated to AFM are presented in two formats: typical $I(v)$ spectra and related second derivative (Figure 5b), which correspond to the average of randomly recorded spectra across the surface of the corresponding AFM image (Figure 5a); a 2D IR map, matching the AFM image and with the intensity being associated to the magnitude of the IR signal recorded at v= 1705 cm^{-1} (Figure 5d).

The $I(v)$ spectra in Figure 5b shows three broad maxima, around 1720 cm^{-1} (peak [2]), 1660 cm^{-1} (peak [3]) and 1590 cm^{-1} (peak [4]), well identified by the negative peaks in the underlying second derivative profile. The average value of v(C=OOH) was reported to be 1723 ± 12 cm^{-1} in a number of aqueous carboxylic acids: high wavenumbers are characteristic of isolated COOH monomers while lower wavenumbers are found in hydrogen bonded COOH,[75] including dimers, as shown for stearic acid Langmuir-Blodgett films.[77] If the broad band around

14

1720 cm^{-1} confirms the presence of a consolidated carboxylic acid network, consequently demonstrating the presence of G-C18:0, its high wavenumber suggests the coexistence of both isolated (1740 cm^{-1}) and hydrogen-bonded (1700 cm^{-1}) COOH groups.[75] The homogeneity of the G-C18:0 coating on the *μm*-scale is demonstrated by the 2D cartography in Figure 5d, recorded at *ν*= 1705 cm^{-1}, thus showing a full COOH coverage of the gold substrates. Noteworthy, the IR map contains localized green spots (e.g., arrow in Figure 5d), sign of a low IR signal that corresponds to surface impurities easily observable on the corresponding AFM image (e.g., arrow on Figure 5c). Finally, the bands around 1660 cm^{-1} and 1590 cm^{-1} are of more straightforward interpretation. The former is attributed to the deformation of adsorbed water (mean value in Ref. [75]: 1643 ± 9 cm^{-1}) while the latter to the asymmetrical stretching of the carboxylate group.

[1]: 1720-1740 cm^{-1} – ν(COOH) [isolated] [3]: 1650 – 1660 cm^{-1} - ν(H$_2$O) [adsorbed]
[2]: 1700-1720 cm^{-1} – ν(COOH) [H-bonding] [4]: 1580 cm^{-1} - ν$_{as}$(COO$^-$)
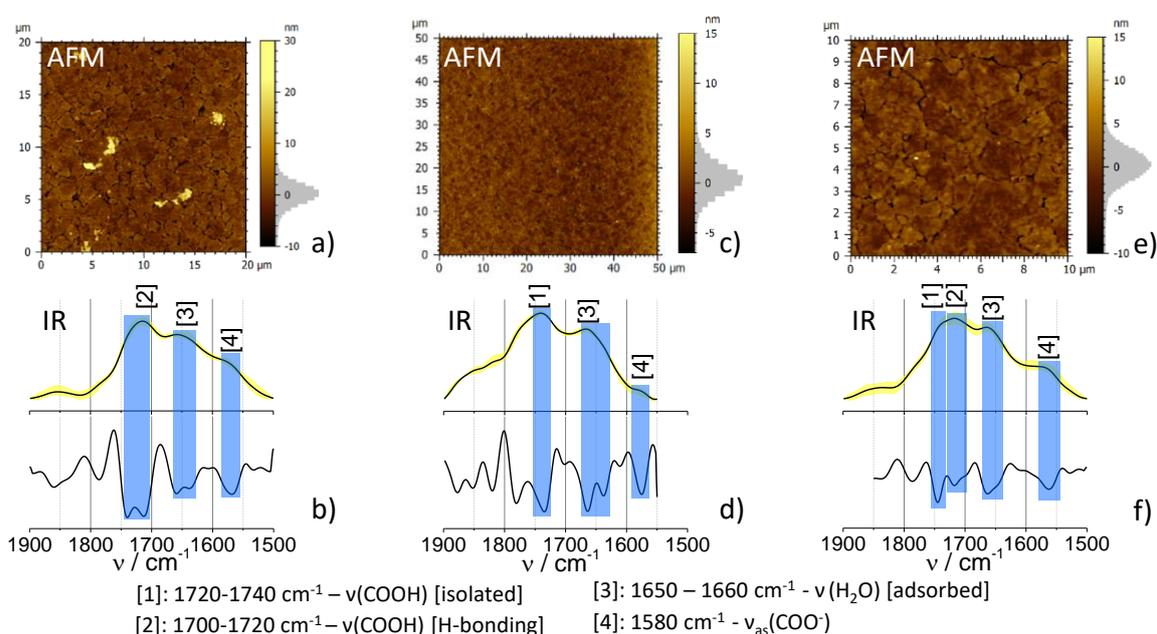
Figure 6 – AFMIR experiments performed on G-C18:0 lipid coated gold substrates. Samples are dip-coated at the optimal conditions of S_w= 0.1 mm/s. AFM image (top) and corresponding normalized averaged IR spectra with second derivative (bottom) of samples a,b) N°166 (100 spectra), c,d) N°174 (15 spectra) and e,f) N°172 (75 spectra). Sample list is given in Table S 3. The background signal (Figure S 5d, average over 15 spectra), measured on a lipid-free gold substrate (Figure S 5b,c), is subtracted from the IR spectrum. IR signals are averages of b) 100, d) 15 and f) 75 spectra randomly collected on their corresponding AFM images. The shaded region surrounding the spectrum corresponds to the dispersion in intensity recorded from multiple spectra.

Figure 6 shows a series of additional AFMIR experiments performed on three additional samples, prepared from both at acidic and basic pH solutions. Besides the faceted structure, intrinsic to the gold substrates, the AFM images are highly homogeneous for all samples on

surfaces going from 100 μm^2 to 2500 μm^2. The corresponding IR signals systematically contain the COOH and COO$^-$ signatures, respectively above 1700 cm^{-1} (peaks [1] and [2]) and around 1590 cm^{-1} (peak [4]). It is not uncommon to find two well-defined signatures either between 1700 and 1720 cm^{-1} (peak [2], Figure 6b) and 1720 and 1740 cm^{-1} (peak [1], Figure 6d) or even coexisting together (peaks [1] and [2], Figure 6f). The relative intensities of peaks [1] and [2] are probably related to a different extent of hydrogen bonding network around the carboxylic acid. However, quantification is a difficult task due to the multicomposite nature of each peak, as shown by the corresponding second derivatives, indicating the presence of both components in the entire 1700 – 1740 cm^{-1} region. Nonetheless, AFMIR can be exploited to draw a qualitative description of the local arrangement of the glucolipids.

G-C18:0 forms interdigitated monolayers, where, to the best of our knowledge, COOH groups are homogeneously distributed on both sides of the membrane (Figure 1). The IR component at 1740 cm^{-1} (isolated COOH) could then be attributed to those G-C18:0 molecules, of which the COOH directly interacts with gold, while the component at 1720 cm^{-1} (COOH engaged in H-bonding) could be attributed to those molecules, of which the COOH group points outward, interacting with external moisture or adjacent glucose moieties. All second derivatives show the lack of a well-defined peak around 1700 cm^{-1} for all samples, thus suggesting that the presence of COOH dimers, as commonly found in multilayers composed of stearic acid,[77] is limited, if not excluded. Since COOH dimers could potentially form between superposed lipid layers, this piece of information, in agreement with ellipsometry, also excludes the presence of multilayers and strengthen the formation of SLM.

AFMIR experiments confirm the presence of a homogeneous G-C18:0 membrane at the *nm-* and *μm*-scale, supporting the homogeneity found by fluorescence microscopy and ellipsometry at higher scales. However, the high homogeneity and lack of defects in most of the AFM images do not allow to confirm the average thickness measured by ellipsometry. The only AFMIR experiment in our possession and which demonstrates the presence of a mostly single G-C18:0 layer, could be performed on a poorly-homogeneous, peripheral, region of a coated Si wafer, shown in Figure S 8 and discussed on Page S19.

AFMIR experiments show that all selected samples contain signals of the COOH and COO$^-$ groups as well as adsorbed water across the entire surface, which is generally homogeneously covered from the *nm-* to the *μm*-scale. These signals, systematically coexisting in aqueous environments of carboxylic acids,[75] provide the unambiguous proof that the G-C18:0 homogeneously covers the entire surface. G-C18:0 coatings are so homogeneous that practically all AFM experiments performed in this work, on both Si wafer and Au substrate,

cannot provide a reliable estimation of their thickness, when classical AFM images performed on SLB display local defects, holes or multilayer adsorption,[23,46,48,51,78] in the absence of which AFM is in fact unable to measure the thickness.[27] Even surface scratching, representing a possible method to peel off part of the coating and measure its thickness with respect to the accessible substrate, is not advised in the case of SLB. It was shown that lipids can be lied down on the surface, instead of being peeled off, they can adsorb onto the tip or they can also diffuse back to fill up the hole soon after scratching.[64–67] Nonetheless, in the lone experiment showing a peripheral region rich in defects, AFMIR shows the presence of mostly single lipid layers, in agreement with the thickness estimations by ellipsometry for those samples displaying $2 < T_h /$ nm < 5 (Figure 2b,d).

Defect-free SLB is a long-date issue[23,24] and such a good, defect-free, homogeneity from the *cm* to the *nm* scales is relatively rare to obtain, all methods taken together.[24,41,45,51] From the Langmuir-Blodgett and vesicle fusion methods, the most common ones in SLB synthesis, it is known that deposition of the lipid gel phase, below the melting temperature, T_m, provides a good SLB homogeneity.[24,41] However, preparing an SLB in the lipid gel phase using the vesicle fusion method decreases the chance to fuse vesicle together, but it increases the risk to find unexploded vesicles on the SLB.[41] The general approach in the vesicle fusion method is then to prepare SLB in the bilayer fluid phase, above the T_m, and then decrease the temperature. However, this process generally provides highly defectuous SLB due to intra-bilayer tensions and cracking.[23,24,47,64] The situation is opposite when preparing SLB from the LB approach. If nearly defect-free SLB could be prepared by LB below the lipid T_m, approaching the gel-to-fluid transition by increasing the temperature induces defects in the SLB.[24] What then determines the best approach is the value of the T_m, that is the type of lipid or lipid formulation. For instance, to prepare a homogeneous SLB at room temperature it could be interesting to employ the LB method in combination with DPPC (L-α-dipalmitoylphosphatidylcholine), which has a T_m of 41°C, while vesicle fusion could be more adapted for DOPC (L-α-dioleoylphosphatidylcholine;), of which the T_m is below 0°C.[23,24]

In this work, we have worked with a glycolipid of which the T_m is close to 37°C,[56] meaning that dip-coating below about 40°C, and in particular at room temperature, constitute the best conditions to obtain highly homogeneous, defect-free, coatings, a fact which is experimentally verified for most samples studied here at $S_w = 0.13 \pm 0.10$ mm/s. Our previous work on the surface self-assembly of sophorolipids did show that the surface energy strongly influences the surface patterns. Inhomogeneous patches and fibrillary aggregates were then found. In the present work, the hypothesis formulated in Figure 1b, according to which the G-

C18:0 interdigitated flat membranes are transferred as such from the solution onto the substrate is actually plausible. This mechanism recalls a coating mechanism similar to what it is described for LB coatings below the lipid T_m, the main difference being that the G-C18:0 membrane is obtained by pre-formed, colloidally-stable, lamellae in solution and not from molecular layers at the liquid-air interface. This assumption is supported by the fact that the optimal concentration to obtain homogeneous supported G-C18:0 layers with thickness between 2 and 5 nm is set at 5 mg/mL, when the colloidal G-C18:0 interdigiated monolayers are fully formed.[20,21] On the contrary, more diluted solutions (1 and 3 mg/mL) provide coatings with thickness below 2 nm, indicative of highly defectuous, or inhomogeneous, coatings. Finally, using a colloidal lamellar soliution instead of vesicles is a clear advantage, because the risk of depositing unexploded vesicles, classical in the vesicle fusion method,[38] is reduced.

When comparing the spin- and dip-coating methods, we find a good homogeneity and the possibility to form single lipid layers. Compared to spin-coating, where the only control parameter is the lipid concentration in solution,[38] dip-coating offers a multitude of parameters (concentration, temperature, withdrawal rate, relative humidity) to control the thickness and homogeneity of the coating. In addition, high lateral pressure during sample spinning were depicted as major causes of SLB inhomogeneity in the spin-coating approach.[48] Dip-coating is a more gentle technique, where anisotropic pressure is not present during coating, thus eliminating additional sources of interdigitation, phase transition or hole formation. Finally, differently than both spin- and horizontal coating evaporation-induced method,[51] dip-coating is easily upscalable and it can be used to coat substrates of virtually any size and morphology, thus being potentially interesting for a broader number of applications.[79]

Conclusion

Glycosylated supported lipid monolayers are prepared by dispersing an aqueous solution of a diluted, colloidally-stable, lamellar phase of a glucolipid obtained by microbial fermentation. A silicon wafer or gold substrate are dipped into a solution containing a dispersed lamellar phase only composed of the glucolipid. Highly homogeneous, crack-free, lipid layers of thickness, $T_h = 2.8 \pm 1.0$ nm are formed at a withdrawal rate of $S_w = 0.13 \pm 0.10$ mm/s. The error on the thickness is obtained by averaging not less than 26 experiments, each performed from acidic or basic pH glucolipid solutions within a broad range of temperature ($T = 30 \pm 10°C$) and relative humidity ($RH\% = 55 \pm 10\%$) conditions, demonstrating the robustness of the present approach.

The quality of the fits associated to the amplitude, $\Psi(\lambda)$, and phase difference, $\Delta(\lambda)$, spectra in ellipsometry experiments is very good for the samples prepared at $S_w = 0.13 \pm 0.10$ mm/s. This supports a high homogeneity of the coatings on the *cm*-scale. Fluorescence microscopy systematically shows a highly homogeneous, poorly contrasted, signal, supporting the homogeneity at the *mm*-scale level. Standard AFM and AFM coupled to infrared spectroscopy (AFMIR) performed on samples prepared at $S_w = 0.13 \pm 0.10$ mm/s show an impressive homogeneity at the *μm*- and *nm*-scale. In general, no distinctive sign of crack, hole or multiple layer is observed. Both randomly-collected single-point and 2D cartographic IR spectra show that the signal of the COOH ($\nu(C=O)$ at 1700-1740 cm^{-1}) and COO$^-$ ($\nu_{s,as}(C=O)$ at 1590 cm^{-1}) groups of the glucolipid are homogeneously distributed across the entire surface for any of the analyzed surfaces.

In summary, the combined use of the dip-coating process with a preformed aqueous glucolipid lamellar phase *de facto* constitutes an ideal approach to prepare defect-free, highly homogeneous, supported lipid layers across the *nm*- to *cm*-scale under practical environmental conditions.

Acknowledgements

References

1 A. Bernardi, J. Jiménez-Barbero, A. Casnati, C. De Castro, T. Darbre, F. Fieschi, J. Finne, H. Funken, K.-E. Jaeger, M. Lahmann, T. K. Lindhorst, M. Marradi, P. Messner, A. Molinaro, P. V. Murphy, C. Nativi, S. Oscarson, S. Penadés, F. Peri, R. J. Pieters, O. Renaudet, J.-L. Reymond, B. Richichi, J. Rojo, F. Sansone, C. Schäffer, W. B. Turnbull, T. Velasco-Torrijos, S. Vidal, S. Vincent, T. Wennekes, H. Zuilhof and A. Imberty, *Chem. Soc. Rev.*, 2013, **42**, 4709–4727.

2 S. M. Brosnan, H. Schlaad and M. Antonietti, *Angew. Chemie - Int. Ed.*, 2015, **54**, 9715–9718.

3 J. Rojo, V. Díaz, J. M. De La Fuente, I. Segura, A. G. Barrientos, H. H. Riese, A. Bernad and S. Penadés, *ChemBioChem*, 2004, **5**, 291–297.

4 T. Weber, V. Chrasekaran, I. Stamer, M. B. Thygesen, A. Terfort and T. K. Lindhorst, *Angew. Chemie - Int. Ed.*, 2014, **53**, 14583–14586.

5 P. M. Claesson, in *Biopolymers at Interfaces, Second Edition*, ed. M. Malmsten, CRC Press, Surfactant., 2003, p. 165.

6 N. Hao, K. Neranon, O. Ramström and M. Yan, *Biosens. Bioelectron.*, 2016, **76**, 113–130.

7   O. Ramström and M. Yan, *Chem. - A Eur. J.*, 2015, **21**, 16310–16317.

8   X. Chen, O. Ramström and M. Yan, *Nano Res.*, 2014, **7**, 1381–1403.

9   B. Kav, A. Grafmueller, E. Schneck and T. R. Weikl, *Nanoscale*, 2020, 17342–17353.

10   T. Fyrner, H. H. Lee, A. Mangone, T. Ekblad, M. E. Pettitt, M. E. Callow, J. A. Callow, S. L. Conlan, R. Mutton, A. S. Clare, P. Konradsson, B. Liedberg and T. Ederth, *Langmuir*, 2011, **27**, 15034–15047.

11   C. Valotteau, C. Calers, S. Casale, J. Berton, C. V. Stevens, F. Babonneau, C. M. Pradier, V. Humblot and N. Baccile, *ACS Appl. Mater. Interfaces*, 2015, **7**, 18086–18095.

12   C. Valotteau, I. M. Banat, C. A. Mitchell, H. Lydon, R. Marchant, F. Babonneau, C.-M. M. Pradier, N. Baccile and V. Humblot, *Colloids Surfaces B Biointerfaces*, 2017, **157**, 325–334.

13   D. Di Iorio, M. L. Verheijden, E. Van Der Vries, P. Jonkheijm and J. Huskens, *ACS Nano*, 2019, **13**, 3413–3423.

14   R. Marchant and I. M. Banat, *Trends Biotechnol.*, 2012, **30**, 558–565.

15   J. D. Desai and I. M. Banat, *Microbiol. Mol. Biol. Rev.*, 1997, **61**, 47–64.

16   C. Valotteau, N. Baccile, V. Humblot, S. Roelants, W. Soetaert, C. V. Stevens and Y. F. Dufrêne, *Nanoscale Horizons*, 2019, **4**, 975–982.

17   M. L. Chen, J. Penfold, R. K. Thomas, T. J. P. P. Smyth, A. Perfumo, R. Marchant, I. M. Banat, P. Stevenson, A. Parry, I. Tucker, I. Grillo, C. ML, M. L. Chen, J. Penfold, R. K. Thomas, T. J. P. P. Smyth, A. Perfumo, R. Marchant, I. M. Banat, P. Stevenson, A. Parry, I. Tucker and I. Grillo, *Langmuir*, 2010, **26**, 18281–18292.

18   M. Chen, C. Dong, J. Penfold, R. K. Thomas, T. J. P. Smyth, A. Perfumo, R. Marchant, I. M. Banat, P. Stevenson, A. Parry, I. Tucker and I. Grillo, *Langmuir*, 2013, **29**, 3912–3923.

19   N. Baccile, F. Babonneau, J. Jestin, G. Pehau-Arnaudet, I. Van Bogaert, G. Péhau-Arnaudet, I. Van Bogaert, G. Pehau-Arnaudet and I. Van Bogaert, *ACS Nano*, 2012, **6**, 4763–4776.

20   N. Baccile, M. Selmane, P. Le Griel, S. Prévost, J. Perez, C. V. Stevens, E. Delbeke, S. Zibek, M. Guenther, W. Soetaert, I. N. A. Van Bogaert and S. Roelants, *Langmuir*, 2016, **32**, 6343–6359.

21   N. Baccile, A.-S. Cuvier, S. Prévost, C. V Stevens, E. Delbeke, J. Berton, W. Soetaert, I. N. A. Van Bogaert and S. Roelants, *Langmuir*, 2016, **32**, 10881–10894.

22   Y. Ishigami, Y. Gama, H. Nagahora, M. Yamaguchi, H. Nakahara and T. Kamata, *Chem. Lett.*, 1987, **16**, 763–766.

23   L. K. Tamm and H. M. McConnell, *Biophys. J.*, 1985, **47**, 105–113.

24   J. Kurniawan, J. F. Ventrici de Souza, A. T. Dang, G. Liu and T. L. Kuhl, *Langmuir*, 2018, **34**, 15622–15639.

25   G. J. Hardy, R. Nayak and S. Zauscher, *Curr. Opin. Colloid Interface Sci.*, 2013, **18**, 448–458.

26   E. T. Castellana and P. S. Cremer, *Surf. Sci. Rep.*, 2006, **61**, 429–444.

27   S. Morandat and K. El Kirat, *Colloids Surfaces B Biointerfaces*, 2007, **55**, 179–184.

28   P. Wessman, A. A. Strömstedt, M. Malmsten and K. Edwards, *Biophys. J.*, 2008, **95**, 4324–4336.

29   Y. K. Lee, H. Lee and J. M. Nam, *NPG Asia Mater.*, 2013, **5**, 1–13.

30   F. Wang, J. H. Seo, G. Luo, M. B. Starr, Z. Li, D. Geng, X. Yin, S. Wang, D. G. Fraser, D. Morgan, Z. Ma and X. Wang, *Nat. Commun.*, 2016, **7**, 10444.

31   T. Fujie, S. Ahadian, H. Liu, H. Chang, S. Ostrovidov, H. Wu, H. Bae, K. Nakajima, H. Kaji and A. Khademhosseini, *Nano Lett.*, 2013, **13**, 3185.

32   B. Yuan, Y. Li, D. Wang, Y. Xie, Y. Liu, L. Cui, F. Tu, H. Li, H. Ji, W. Zhang and X. Jiang, *Adv. Funct. Mater.*, 2010, **20**, 3715.

33   E. Kang, J. Ryoo, G. S. Jeong, Y. Y. Choi, S. M. Jeong, J. Ju, S. Chung, S. Takayama and S. H. Lee, *Adv. Mater.*, 2013, **25**, 2167.

34   M. Wlodek, M. Kolasinska-Sojka, M. Szuwarzynski, S. Kereïche, L. Kovacik, L. Zhou, L. Islas, P. Warszynski and W. H. Briscoe, *Nanoscale*, 2018, **10**, 17965–17974.

35   J. Fleddermann, E. Diamanti, S. Azinas, M. Košutić, L. Dähne, I. Estrela-Lopis, M. Amacker, E. Donath and S. E. Moya, *Nanoscale*, 2016, **8**, 7933–7941.

36   H. A. Rinia, R. A. Demel, J. P. van der Eerden and B. de Kruijff, *Biophys. J.*, 1999, **77**, 1683–93.

37   E. Kalb, S. Frey and L. K. Tamm, *Biochim. Biophys. Acta*, 1992, **1103**, 307–316.

38   G. Csùcs and J. J. Ramsdem, *Biochim. Biophys. Acta*, 1998, **1369**, 61–70.

39   M. C. Howland, A. W. Szmodis, B. Sanii and A. N. Parikh, *Biophys. J.*, 2007, **92**, 1306–17.

40   S. J. Johnson, T. M. Bayerl, D. C. McDermott, G. W. Adam, A. R. Rennie, R. K. Thomas and E. Sackmann, *Biophys. J.*, 1991, **59**, 289–294.

41   T. K. Lind and M. Cárdenas, *Biointerphases*, 2016, **11**, 020801.

42   B. Sironi, T. Snow, C. Redeker, A. Slastanova, O. Bikondoa, T. Arnold, J. Kleine and W. H. Briscoe, *Soft Matter*, 2016, **12**, 3877–3887.

43   I. Möller and S. Seeger, *J. Mater. Chem. B*, 2015, **3**, 6046–6056.

44   R. Caminiti, G. Caracciolo, M. Pisani and P. Bruni, *Chem. Phys. Lett.*, 2005, **409**, 331–336.

45   U. Mennicke and T. Salditt, *Langmuir*, 2002, **18**, 8172–8177.

46   L. Krapf, M. Dezi, W. Reichstein, J. Köhler and S. Oellerich, *Colloids Surfaces B Biointerfaces*, 2011, **82**, 25–32.

47   A. C. Simonsen and L. A. Bagatolli, *Langmuir*, 2004, **20**, 9720–9728.

48   A. Dols-Perez, L. Fumagalli and G. Gomila, *Colloids Surfaces B Biointerfaces*, 2018, **172**, 400–406.

49   J. Generosi, C. Castellano, D. Pozzi, A. Congiu Castellano, R. Felici, F. Natali and G. Fragneto, *J. Appl. Phys.*, 2004, **96**, 6839–6844.

50   L. Perino-Gallice, G. Fragneto, U. Mennicke, T. Salditt and F. Rieutord, *Eur. Phys. J. E*, 2002, **8**, 275–282.

51 M. Le Berre, Y. Chen and D. Baigl, *Langmuir*, 2009, **25**, 2554–2557.

52 N. Baccile, C. Seyrig, A. Poirier, S. A. Castro, S. L. K. W. Roelants and S. Abel, *Green Chem.*, 2021, **23**, 3842–3944.

53 J. Peyre, A. Hamraoui, M. Faustini, V. Humblot and N. Baccile, *Phys. Chem. Chem. Phys.*, 2017, **19**, 15227–15238.

54 M. Faustini, M. Faustini, B. Louis, P. A. Albouy, M. Kuemmel and D. Grosso, *J. Phys. Chem. C*, 2010, **114**, 7637–7645.

55 K. M. J. Saerens, J. Zhang, L. Saey, I. N. A. Van Bogaert and W. Soetaert, *Yeast*, 2011, **28**, 279–292.

56 G. Ben Messaoud, P. Le Griel, S. Prévost, D. H. Merino, W. Soetaert, S. L. K. W. Roelants, C. V. Stevens and N. Baccile, *Soft Matter*, 2020, **16**, 2528–2539.

57 G. Ben Messaoud, P. Le Griel, D. H. Merino and N. Baccile, *Soft Matter*, 2020, **16**, 2540–2551.

58 R. Nagarajan, *Chem. Eng. Commun.*, 1987, **55**, 251–273.

59 N. Baccile and V. Cristiglio, *Langmuir*, 2020, **36**, 2191–2198.

60 K. Kolahdouzan, J. A. Jackman, B. K. Yoon, M. C. Kim, M. S. Johal and N. J. Cho, *Langmuir*, 2017, **33**, 5052–5064.

61 S. M. Baumler, A. M. McHale and G. J. Blanchard, *J. Electroanal. Chem.*, 2018, **812**, 159–165.

62 F. Gołek, P. Mazur, Z. Ryszka and S. Zuber, *Appl. Surf. Sci.*, 2014, **304**, 11–19.

63 J. M. Solletti, *J. Vac. Sci. Technol. B Microelectron. Nanom. Struct.*, 1996, **14**, 1492.

64 A. Charrier and F. Thibaudau, *Biophys. J.*, 2005, **89**, 1094–1101.

65 M. F. Luo, Y. L. Yeh, P. L. Chen, C. H. Nien and Y. W. Hsueh, *J. Chem. Phys.*, , DOI:10.1063/1.2194539.

66 S. Garcia-Manyes, O. Domènech, F. Sanz, M. T. Montero and J. Hernandez-Borrell, *Biochim. Biophys. Acta*, 2007, **1768**, 1190–8.

67 N. C. Santos, E. Ter-Ovanesyan, J. A. Zasadzinski and M. A. R. B. Castanho, *Biophys. J.*, 1998, **75**, 2119–2120.

68 A. Dazzi, R. Prazeres, F. Glotin and J. M. Ortega, *Opt. Lett.*, 2005, **30**, 2388.

69 F. Lu, M. Jin and M. A. Belkin, *Nat. Photonics*, 2014, **8**, 307–312.

70 F. Lu and M. A. Belkin, *Opt. Express*, 2011, **19**, 19942.

71 A. Dazzi, R. Prazeres, F. Glotin, J. M. Ortega, M. Al-Sawaftah and M. de Frutos, *Ultramicroscopy*, 2008, **108**, 635–641.

72 T. Awatani, H. Midorikawa, N. Kojima, J. Ye and C. Marcott, *Electrochem. commun.*, 2013, **30**, 5–8.

73 J. R. Felts, S. Law, C. M. Roberts, V. Podolskiy, D. M. Wasserman and W. P. King, *Appl. Phys. Lett.*, 2013, **102**, 152110.

74   A. Deniset-Besseau, C. B. Prater, M. J. Virolle and A. Dazzi, *J. Phys. Chem. Lett.*, 2014, **5**, 654–658.

75   J. J. Max and C. Chapados, *J. Phys. Chem. A*, 2004, **108**, 3324–3337.

76   N. Baccile, R. Noiville, L. Stievano and I. Van Bogaert, *Phys. Chem. Chem. Phys.*, 2013, **15**, 1606–1620.

77   F. Kimura, J. Umemura and T. Takenaka, *Langmuir*, 1986, **2**, 96–101.

78   S. Morandat, S. Azouzi, E. Beauvais, A. Mastouri and K. El Kirat, *Anal. Bioanal. Chem.*, 2013, **405**, 1445–1461.

79   J. Puetz and M. A. Aegerter, in *Sol-Gel Technologies for Glass Producers and Users*, Springer, Boston, MA, 2004, pp. 37–48.

Legend of Figures in the Supporting Information

Figure S 1 - Scheme and images of the dip-coating system and apparatus

Figure S 2 – a) Scheme of multilayer model employed to fit the fit $\Psi(\lambda)$ and $\Delta(\lambda)$ spectra obtained by ellipsometry on samples coated on commercial silicon wafers. The typical fitted $\Psi(\lambda)$ and $\Delta(\lambda)$ spectra for selected samples are given for samples (Table S 3): b) commercial Si wafer control, c) N° 203, d) N° 176, e) N° 167. Typical good (d-e) and poor (c) quality fits are given on purpose.

Table S 1 – Fitted values of the thickness, T_h, and fit quality for Si wafer control and samples shown Figure S 2. T_h is the average of the thickness values obtained with refractive index of 1.4 an 1.7 (lower and upper maximum reported for homogeneous, dense, lipid bilayers).

Figure S 3 - a) Scheme of multilayer model employed to fit the fit $\Psi(\lambda)$ and $\Delta(\lambda)$ spectra obtained by ellipsometry on samples coated on commercial Au substrates. The typical fitted $\Psi(\lambda)$ and $\Delta(\lambda)$ spectra for selected samples are given for samples (Table S 3): b) commercial Au substrate control, c) N° 158.

Table S 2 - Fitted values of the thickness, T_h, and fit quality for Au substrate control and sample shown Figure S 2. T_h is the average of the thickness values obtained with refractive index of 1.4 an 1.7 (lower and upper maximum reported for homogeneous, dense, lipid bilayers).

Figure S 4 – a) Evolution of T_h as a function of the G-C18:0 lipid concentration in the parent solution. The specific conditions of pH, S_w, RH% and T are given on the figures. The conditions for each plotted sample are given in Table S 3. Samples N° are 99-139, 155-157, 159, 161, 163, 165, 167, 171. b) Evolution of T_h as a function of the relative humidity in the dip-coating chamber. The specific conditions of solution concentration, C, S_w and T are given on the figures. Red circles and black stars respectively correspond to the pH of the parent solution. The conditions for each plotted sample are given in Table S 3. Sample N° associated to red circles are: 155-157, 159, 161, 163, 165, 167, 171, while sample N° for black stars are: 41, 42, 50, 54-64, 69, 142-143, 145-154, 174, 176

Table S 3 – Full list of samples prepared in this work. The concentration, C, and pH are meant for the parent solution before dip-coating. Temperature, T, and relative humidity, RH%, are meant inside the dip-coating chamber, during dip-coating. S_w: withdrawal speed, T_h: thickness of the lipid film; σ: standard deviation; Typical fit of poor and good quality are respectively given, as an example, in Figure S 2c and Figure S 2d. Green lines: samples at pH 6 plotted in Figure 2 in the main text; Red lines: samples at pH 9 plotted in Figure 2 in the main text.

Table S 4 – Surface roughness calculated from the h(d) profiles (h is the height in nm and d is the distance in μm) for samples corresponding to AFM images in Figure 4 (Sample list is given in Table S 3) and to the

bare control silicon substrate in Figure S 5a. For sample 176 in profile Figure 4a), only the 13 < d (μm) < 40 region is considered to avoid the peak and valley artifacts. R_q: root mean squared roughness; R_{sk}: skewness; R_v: valley roughness, lowest value of height; R_p: peak roughness, highest value of height; Δ_{RpRv}: peak-to-valley roughness, largest height amplitude. In the formulas, n is the number of height values in the h(d) profiles.

Figure S 5 – a) AFM image and corresponding height –distance, $h(d)$, profile (white segmeted line) measured on a commercial Si wafer control substrate. b) Large-scale AFM image of the Au control substrate. c) Magnified AFM image of the Au control substrate showing the typical mosaic-like structure composed of Au (111) crystalline domains (white segmented lines). d) IR spectrum measured by AFMIR experiments on the Au substrate. The spectrum is the resul of 15 averaged spectra collected randomly on the corresponding AFM image in b). The gold substrate control displays no IR signal in the IR region between 1900 and 1500 cm^{-1}.

Figure S 6 – a-d) Fluorescence microscopy and e-f) ellipsometry experiments. Sample N° 174 (a) and N° 173 are respectively prepared on gold and Si wafer substrates and they are dip-coated from the same parent solution employing the same conditions. Similarly, sample N° 166 (c,e) and N° 167 (d,f) are respectively prepared on gold and Si wafer substrates and they are dip-coated from the same parent solution employing the same conditions. Exact conditions for each samples are given in Table S 3.

Table S 5 - Fitted values of the thickness, T_h, and fit quality for samples N° 166 and N° 167, respectively prepared using Au and Si wafer substrates from the same G-C18:0 lipid solution and using the same dip-coating parameters (experimental details are in Table S 3). T_h is the average of the thickness values obtained with refractive index of 1.4 an 1.7 (lower and upper maximum reported for homogeneous, dense, lipid bilayers).

Figure S 7 - Non-normalized IR spectra corresponding to the AFMIR experiment performed on G-C18:0 lipid-coated gold substrates (Sample N°175, Table S 3) dipped at the optimal conditions of S_w= 0.1 mm/s. Each spectrum is the average of 5 spectra, randomly collected on the AFM image presented in Figure 5a in the main text. The Au control background signal is presented on Figure S 5d and measured on a lipid-free gold substrate (Figure S 5b,c).

Figure S 8 – Coupled AFMIR experiment performed on sample N° 58 (Table S *3*) prepared on a Si wafer substrate. a) AFM image and corresponding thickness profile (green line), $h(d)$, measured along the white thick line. b) 2D IR cartography recorded at 1710 cm^{-1} and corresponding to the AFM image in a). Segmented regions labelled *1*, *2* and *3* in a) and b) correspond to the Si wafer substrate (*1*-labelled), single-layer (*2*-labelled) and double-layer (*3*-labelled) G-C18:0 coating.

Homogeneous Supported Monolayer from Microbial Glycolipid Biosurfactant

Niki Baccile,[a,*] Anyssa Derj,[a] Cédric Boissière,[a] Vincent Humblot,[b,c] Ariane Deniset-Besseau[d]

[a] Sorbonne Université, Centre National de la Recherche Scientifique, Laboratoire de Chimie de la Matière Condensée de Paris, LCMCP, F-75005 Paris, France

[b] Sorbonne Université, Laboratoire de Réactivité de Surface (LRS), UMR CNRS 7197, 4 place Jussieu, Paris, F-75005, France

[c] Current address : FEMTO-ST Institute, UMR CNRS 6174, Université Bourgogne Franche-Comté, 15B avenue des Montboucons, 25030 Besançon Cedex, France

[d] Université Paris-Saclay, CNRS, Institut de Chimie Physique, UMR 8000, 91405, Orsay, France

Experimental Section

Chemicals. The microbial monounstaurated glucolipid G-C18:1 has been produced at a production rate of ~ 0.5 $gL^{-1}h^{-1}$ in a bioreactor system using a modified strain (*ΔugtB1*) of the yeast *Starmerella bombicola* and based on the experimental conditions described by Saerens et al.[1] Thereafter, the fully saturated G-C18:0 (M_w = 462.6 g.mol^{-1}), employed in this work (Figure 1a in the main text), is obtained from G-C18:1 by a catalytic hydrogenation reaction described elsewhere.[2] The full characterization of G-C18:0 is reported in ref.[2]. 1,2-dioleoyl-sn-glycero-3-phosphoethanolamine-N-(lissamine rhodamine B sulfonyl) ammonium salt, (*Liss*, M_w= 1301.7 g.mol^{-1}, λ_{abs}= 560 nm, λ_{em}= 583 nm), is purchased by Avanti® Polar, Inc. Base (NaOH) solutions and acetic acid (Sigma Aldrich) are used with the following molarities: 5 M, 1 M, 0.5 M and 0.1 M NaOH. All solutions have been prepared with Milli-Q-grade water.

Substrates. Boron-doped one-sided polished Si(100) wafers (thickness 0.7 mm) are cut in approximately 3 cm x 1.5 cm plates using a diamond pen, then washed using ethanol 96% and dried using nitrogen gas. Silicon wafers have a typical native SiO_2 coating of few Å. Au(111) substrates (1 cm² x 1 cm²), purchased from Arrandee (Werther, Germany), are composed of a 1 mm SiO_2 glass substrate coated with 50 Å thick chromium and 200 nm thick Au layers. Gold substrates are annealed using a butane flame to ensure good crystallinity and eventually rinsed with 96% ethanol under sonication during 5 min.

Solutions. We initially prepare a stock solution (*V*= 10 mL) of G-C18:0 at *C*= 5 mg/mL and pH ~9.3, adjusted using few (~1-3) µL of a 5 M NaOH solution. Stock solution is employed to prepare three solutions of 3 mL each at concentration *C*= 5 mg/mL, 3 mg/mL, 1 mg/mL, of which the pH is lowered to about 6 using few µL (~5-10) of a 0.1 M HCl solution. These solutions are used as such for dip-coating experiments.

For fluorescence emission experiments, a methanolic solution of *Liss* (4 mg/mL, 3.08 mM) is added to the sample solution prior to dip coating so that the final molar ratio between G-C18:0 and *Liss* is, G-C18:0:*Liss*= 200:1. *Liss* is a standard marker for lipid bilayers for it's lipid backbone is assumed to intercalate in the lipid bilayer without perturbing it, when the lipid:dye molar ratio ≥100.[3,4]

Dip-coating. Dip coating is performed using a ACEdip 2.0 dip-coater (SolGelWay, France), which allows a precise control of the withdrawal rate, S_w, between 0.001 mm/s to 30 mm/s and temperature, *T*. Relative humidity, *RH%*, in the dip-coating chamber is controlled via the Gas

53   Flow Controller ACEflow 2.0 (SolGelWay, France). The dip-coating apparatus described in

54   Figure S 1. Silicon wafer of approximate size of 1.5 cm x 3 cm are directly plunged in the lipid

55   solution, while gold substrates (1 cm x 1 cm) are plunged after solidarization on the silicon

56   wafer (at about 5 mm from the bottom).

57

58   *Preparation of samples*. G-C18:0 lipid is known to undergo a pH-driven micelle-to-lamellar

59   phase transition:[2,5] at pH 9 and concentration below 5 mg/mL, G-C18:0 assembles mainly into

60   a micellar phase, while at pH 6, it assembles into infinitely wide planar bilayers. We then

61   employ two dipping strategies. In method 1, we employ a lipid solution at pH 9 while in method

62   2 the lipid solution is at pH 6. In both cases, temperature and relative humidity of the dip-

63   coating chamber are respectively varied between 20 and 60°C and 5 and 95 RH%.

64   *Ellipsometry*. Spectroscopic ellipsometry analyses are recorded with a UV-NIR (193-1690 nm)

65   variable angle spectroscopic ellipsometer (VASE) M2000DI from J. A. Woollam Co., Inc. To

66   increase the precision of the measurement, data are acquired at three different incident angles

67   (60°, 65° and 70°) per location, close to the Brewster angles of silicon. The beam surface area

68   is between 0.15 cm^2 and 0.20 cm^2, thus averaging the data over a broad surface. Each deposited

69   lipid film is measured at three different locations. Data acquisition is performed with

70   CompleteEASE™ (Version 5.19, 2016) software by J. A. Woollam Co., Inc. Two substrates

71   are used to deposit the lipid thin film, Si wafers and Au plates.

72

73   *Ellipsometry data analysis*. Ellipsometry is a technique, which measures the change of

74   polarization states of an incident polarized beam after reflection from a sample. In particular, it

75   provides access to the complex reflectance ratio, $\rho(\lambda)$ (λ is the wavelength of the incident light),

76   which may be parametrized by the amplitude, $\Psi(\lambda)$ and the phase difference, $\Delta(\lambda)$, of the p

77   (parallel to the plane of incidence) and s (perpendicular to the plane of incidence) polarized

78   reflectivities, r_p and r_s according to $\rho = \tan \Psi \cdot e^{i\Delta} = r_p/r_s$.[6] To maximize the difference in r_p and

79   r_s, experiments are performed close to the Brewster angle. Ellipsometry measures $\Psi(\lambda)$ and

80    $\Delta(\lambda)$, which can be related to refractive index, RI, of the material and to its thickness, T_h, by

81   adapted models.

82   Modelling and fitting of the $\Psi(\lambda)$ and $\Delta(\lambda)$ to recover the thickness, T_h, of the deposited

83   thin film is done with the analysis tool of the CompleteEASE™ (Version 5.19, 2016) software

84   by J. A. Woollam Co., Inc. The detailed approach, some typical experimental and fitted $\Psi(\lambda)$

85   and $\Delta(\lambda)$ spectra and corresponding results of the fits are given in Figure S 2 for the Si substrate

86 and in Figure S 3 for the Au plate. Modelling is performed via the approach suggested in the

87 CompleteEASE™ data analysis manual (Ed. 2004-2011). In short, the Si substrate is modelled

88 with a general oscillator (*Gen-Osc*) layer model (p. 131, data analysis manual), typical for

89 absorbing thin films, while the native SiO_2 oxide top layer is modelled with two layer models,

90 a higher index interface layer (*Intr_Jaw*) and silica layer (*SiO2_Jaw*), respectively of thickness

91 1 nm and 0.52 nm. *Gen_Osc*, *Intr_Jaw* and *SiO2_Jaw* are files containing the optical constants

92 for each layer and available in the CompleteEASE™ library (JAW stands for J. A. Woollam).

93 They are the best-suited files to fit satisfactorily the $\Psi(\lambda)$ and $\Delta(\lambda)$ spectra of the reference, lipid-

94 free, Si wafer (Figure S 2a,b and Table S 1). The Au plate is modelled with a SiO_2 substrate

95 (*Glass_slide*), a chrome layer of T_h= 5 nm (*Cr*) and a gold layer of T_h= 200 nm (*Au_nk1*). The

96 three layers correspond to the known composition of Au plates provided by the manufacturer.

97 *Glass_slide*, *Cr* and *Au_nk1* are the best suited optical constants-containing files to obtain a

98 good fit of the reference, lipid-free, Au plate (Figure S 3a,b and Table S 2).

99   The dip-coated lipid layer is modelled with a Cauchy model (Figure S 2a), classically

100 employed for transparent thin films, which is the case for the lipids employed in the UV-Vis-

101 NIR range. The refractive index, RI, of the lipid layer could be fixed. However, the actual values

102 of RI are difficult to determine with precision for thin (< 10 nm) films, due to uncertainty about

103 the actual surface density of the film. At the same time, keeping RI as a variable under these

104 conditions is not appropriate either, due to high chance to obtain physically unreal values. In

105 this work, we make the following choice: we assumed to have a homogeneous coating and, for

106 this reason, we systematically fit $\Psi(\lambda)$ and $\Delta(\lambda)$ of the lipid-coated supports using the lower and

107 upper limits of RI values known for lipid bilayers,[7,8] respectively RI= 1.4 and RI= 1.7, whereas

108 the refractive index of glucose is also contained in this interval. In case of good quality fits,

109 only those values of the thickness above 2 nm were considered to have a physical meaning and

110 in agreement with a homogeneous mono, or multilayer, coating. The value of 2 nm is somewhat

111 arbitrary but SAM of glycolipids bearing between one and three carbohydrate units were shown

112 to have thickness (by ellipsometry) between 2.7 and 3.0 nm.[9,10] On the other hand, 2 nm is the

113 lowest limit for a G-C18:0 interdigitated layer having a possible tilt angle of about 60°, a higher

114 limit in self-assembled monolayers,[11–14] with respect to the normal vector. Values of thickness

115 below 2 nm, although analytically correct, were not considered compatible with a homogeneous

116 coating. The refractive index employed in the fit was probably not realistic, that is not

117 compatible with a homogeneous dense coating, the underlying hypothesis of the Cauchy fitting

118 model. The final thickness is taken to be as an average value with an error resulting from the

119 extreme refractive indexes. On average, the experimental relative error on the thickness value
120 per each sample is about 13%.

121 Table S 1 and Table S 2 report, for selected samples, the fitted thickness at RI= 1.4 and
122 RI= 1.7, the average value and the error. Table S 3 provides the entire set of samples analyzed
123 in this work by ellipsometry: the experimental conditions, the average value of the fitted
124 thickness at RI= 1.4 and RI= 1.7, T_h, the standard deviation, σ, as well as the quality of the fit.

125 When the fit perfectly matches the experimental data within the imposed constraints, we
126 consider it to be a good fit and the corresponding T_h value to be reliable. Figure S 2d,e show
127 typical examples of good quality fits giving reliable thickness values (samples 176 and 167 in
128 Table S 1) on selected samples. However, it may happen that, even if the fit is of good quality,
129 the thickness value assumes physically unreal values, below about 2 nm (samples 99-131 in
130 Table S 3). It should be noted that the thickness of the G-C18:0 interdigitated layer can be
131 calculated to be about 3.0 nm by applying the Tanford formula ($L = 1.54 + 1.265 \times n$, L being
132 the length of the aliphatic chain and n the number of methylene groups)[15] to an effective C16
133 aliphatic chain and taking 8 Å as the size of a single glucose molecule.[16] This estimation is in
134 agreement with the experimental values measured by SAXS in aqueous solution between pH 6
135 and 7 and found to be in the order of 3.6 nm.[2,5] In this situation, the coating has either not
136 occurred or the surface coverage is only partial. In other cases, fits are of poor quality, as shown
137 in Figure S 2c, and the corresponding thickness (e.g., sample 203 in Table S 1) is generally
138 unreliable. This often occurs for thick, poorly homogeneous, coatings.

139

140 *Fluorescence microscopy*. Fluorescence microscopy in reflection configuration is performed
141 on substrates dip-coated in a lipid solution containing the *Liss* fluorophore. We use an Axio
142 Observer D1, Carl Zeiss microscope, equipped with a CCD camera and a multi-wavelength
143 light source. Samples are excited at 530-560 nm and the emission is detected between 571- 631
144 nm.

145

146 *Atomic Force Microscopy (AFM)*. AFM images of dried surfaces were recorded using a
147 MultiMode 8-HR AFM microscope from Bruker Instruments Inc. To avoid tip and sample
148 damages, topographic images were taken in the QNM Air mode. SCANASYST-Air tips from
149 Bruker (resonance frequency 70 kHz, force constant 0.4 N/m) have been used. Images were
150 obtained at a constant speed of 1 Hz with a resolution of 512 lines and 512 pixels each. The raw
151 data were processed using the imaging processing software NanoScope Analysis, mainly to
152 correct the background slope between the tip and the surfaces.

153

IR nanospectroscopy, AFMIR: Atomic Force Microscopy coupled to Infrared Spesctroscopy.
The principle of AFMIR is well described in several recent papers.[17–21] To sum-up, an AFM is
coupled to an IR pulsed laser to perform chemical analysis of a sample at the nanoscale. The
technique allows performing IR analysis thanks to the tip in contact with the sample. It acquires
simultaneously topographical image and IR map at a specific absorption band as well as local
IR spectra. The technique is used in resonance-enhanced mode using a top-down illumination
(NanoIR2, Anasys Instruments, CA USA). The laser is a multi-chip quantum cascade laser
QCL (MIRCAT, Daylight solution, CA USA) ranging from 1510 cm^{-1} to 1920 cm^{-1}. The laser
repetition rate ranges from 1 kHz to 2 MHz and is chosen to match the contact resonant
frequency of the AFM cantilever. A gold coated probe was used (MikroMasch : HQ:CSC38/Al-
BS-50 - spring constant 0.03 N/m – resonance around 190 kHz). The spectra were collected
with 1 cm^{-1} spectral resolution.
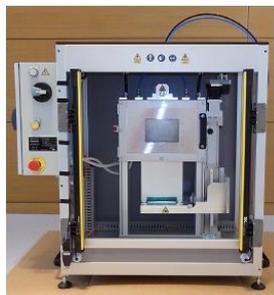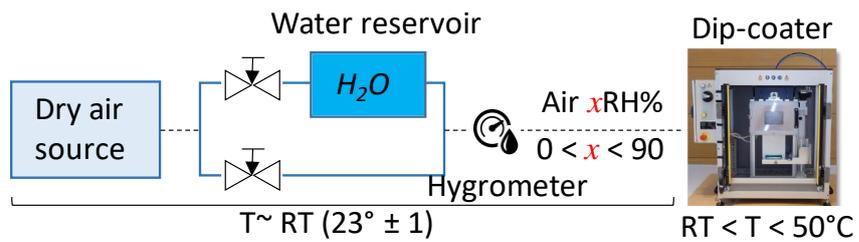
Dip-coater
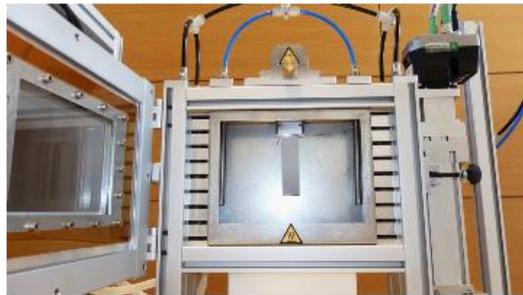
Temperature-stabilized closed dip-coating chamber

166

167   **Figure S 1 - Scheme and images of the dip-coating system and apparatus**

168

Multilayer model to fit ellipsometry spectra with <u>SILICON</u> substrate
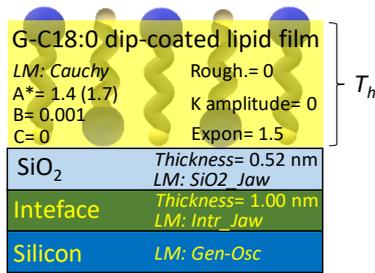
G-C18:0 dip-coated lipid film
LM: Cauchy
A*= 1.4 (1.7)   Rough.= 0
B= 0.001   K amplitude= 0
C= 0   Expon= 1.5

SiO₂   *Thickness= 0.52 nm*
        LM: SiO2_Jaw
Inteface   *Thickness= 1.00 nm*
            LM: Intr_Jaw
Silicon   *LM: Gen-Osc*

T_h

LM: Layer Model in Woollam EASE Sotware library

*: A correponds to the refractive index, RI. Fits are performed with RI= 1.4 and RI= 1.7

Cauchy equation: $n(\lambda) = A + \dfrac{B}{\lambda^2} + \dfrac{C}{\lambda^4}$

Fitted parameter: lipid thickness, T_h

a)

b)

c)

d)

e)
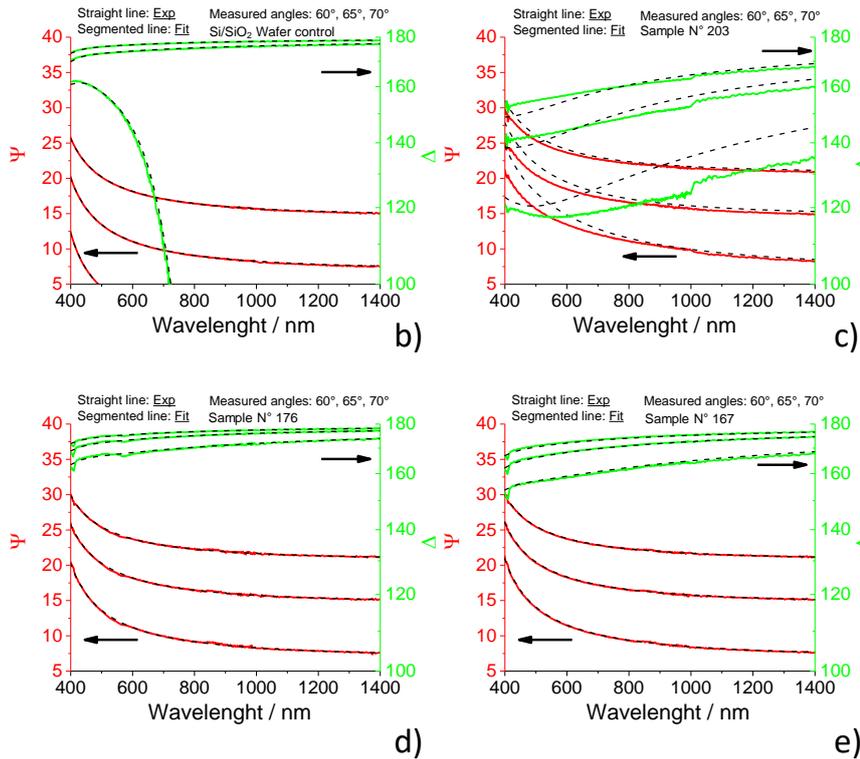
169

170 **Figure S 2 – a) Scheme of multilayer model employed to fit the fit $\Psi(\lambda)$ and $\Delta(\lambda)$ spectra obtained by**

171 **ellipsometry on samples coated on commercial silicon wafers. The typical fitted $\Psi(\lambda)$ and $\Delta(\lambda)$ spectra for**

172 **selected samples are given for samples (Table S 3): b) commercial Si wafer control, c) N° 203, d) N° 176, e)**

173 **N° 167. Typical good (d-e) and poor (c) quality fits are given on purpose.**

174

175 **Table S 1 – Fitted values of the thickness, T_h, and fit quality for Si wafer control and samples shown Figure**

176 **S 2. T_h is the average of the thickness values obtained with refractive index of 1.4 an 1.7 (lower and upper**

177 **maximum reported for homogeneous, dense, lipid bilayers).**

Sample N°	Substrate	T_h (RI= 1.4)	T_h (RI= 1.7)	Average T_h	Fit quality
Silicon/SiO₂ wafer control	-	-	-	0	Good
203	Silicon/SiO₂	20.66	14.14	10.40 ± 3.01	Poor
176	Silicon/SiO₂	2.25	1.70	1.98 ± 0.39	Good
167	Silicon/SiO₂	5.66	4.26	4.96 ± 0.99	Good

178

Multilayer model to fit ellipsometry spectra with <u>GOLD</u> substrate
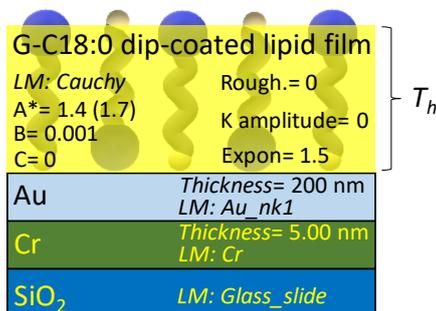
G-C18:0 dip-coated lipid film
LM: Cauchy   Rough.= 0
A*= 1.4 (1.7)   K amplitude= 0
B= 0.001
C= 0   Expon= 1.5

T_h

Au   *Thickness= 200 nm*
      LM: Au_nk1

Cr   *Thickness= 5.00 nm*
      LM: Cr

SiO$_2$ *LM: Glass_slide*

LM: Layer Model in Woollam EASE Sotware library

*: A correponds to the refractive index, RI. Fits are performed with RI= 1.4 and RI= 1.7

Cauchy equation: $n(\lambda) = A + \dfrac{B}{\lambda^2} + \dfrac{C}{\lambda^4}$

Fitted parameter: lipid thickness, T_h

a)

b)

c)

179
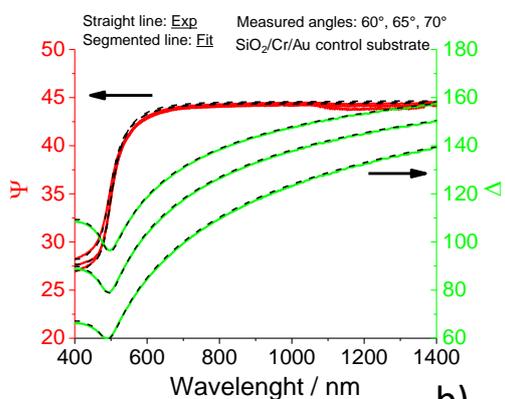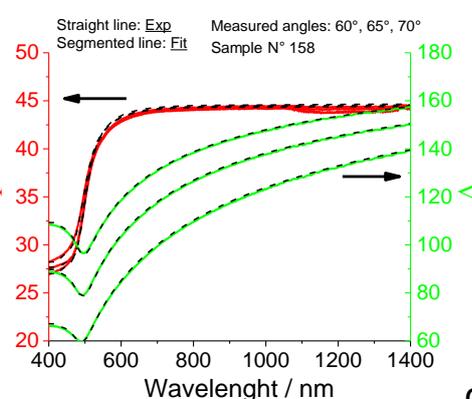
180 **Figure S 3 - a) Scheme of multilayer model employed to fit the fit $\Psi(\lambda)$ and $\Delta(\lambda)$ spectra obtained by**
181 **ellipsometry on samples coated on commercial Au substrates. The typical fitted $\Psi(\lambda)$ and $\Delta(\lambda)$ spectra for**
182 **selected samples are given for samples (Table S 3): b) commercial Au substrate control, c) N° 158.**

183

184 **Table S 2 - Fitted values of the thickness, T_h, and fit quality for Au substrate control and sample shown**
185 **Figure S 2. T_h is the average of the thickness values obtained with refractive index of 1.4 an 1.7 (lower and**
186 **upper maximum reported for homogeneous, dense, lipid bilayers).**

Sample N°	Substrate	T_h (RI= 1.4)	T_h (RI= 1.7)	Average T_h	Fit quality
SiO$_2$/Cr/Au control substrate	-	-	-	0	Good
158	SiO$_2$/Cr/Gold	13.4	9.08	11.24 ± 3.05	Good

187

188

189

190

Figure S 4 – a) Evolution of T_h as a function of the G-C18:0 lipid concentration in the parent solution. The specific conditions of pH, S_w, $RH\%$ and T are given on the figures. The conditions for each plotted sample are given in Table S 3. Samples N° are 99-139, 155-157, 159, 161, 163, 165, 167, 171. b) Evolution of T_h as a function of the relative humidity in the dip-coating chamber. The specific conditions of solution concentration, C, S_w and T are given on the figures. Red circles and black stars respectively correspond to the pH of the parent solution. The conditions for each plotted sample are given in Table S 3. Sample N° associated to red circles are: 155-157, 159, 161, 163, 165, 167, 171, while sample N° for black stars are: 41, 42, 50, 54-64, 69, 142-143, 145-154, 174, 176

202 **Table S 3 – Full list of samples prepared in this work. The concentration, *C*, and pH are meant for the**
203 **parent solution before dip-coating. Temperature, *T*, and relative humidity, *RH%*, are meant inside the dip-**
204 **coating chamber, during dip-coating. S_w: withdrawal speed, T_h: thickness of the lipid film; σ: standard**
205 **deviation; Typical fit of poor and good quality are respectively given, as an example, in Figure S 2c and**
206 **Figure S 2d. Green lines: samples at pH 6 plotted in Figure 2 in the main text; Red lines: samples at pH 9**
207 **plotted in Figure 2 in the main text.**

Sample N°	Substrate	C / mg/mL	pH	T / •C	RH%	S_w / mm/s	T_h / nm	σ / nm	Fit quality
11	Si wafer	5	9	27	56	1.000	19.03	5.65	Poor
12	Si wafer	5	9	27	35	1.000	19.03	3.28	Poor
18	Si wafer	5	9	27	56	1.000	25.85	5.79	Poor
24	Si wafer	5	9	27	1	1.000	17.19	3.26	Good
25	Si wafer	5	9	23	4	1.000	23.60	3.83	Poor
26	Si wafer	5	9	23	3	1.000	13.64	2.68	Good
27	Si wafer	5	9	23	2	1.000	0.20	0.04	Good
41	Si wafer	5	9	34	58	0.075	3.72	0.74	Good
42	Si wafer	5	9	33	58	0.050	5.25	1.04	Good
50	Si wafer	5	9	22	53	0.100	2.16	0.42	Good
54	Si wafer	5	9	23	53	0.075	2.14	0.42	Good
55	Si wafer	5	9	24	53	0.050	2.22	0.43	Good
56	Si wafer	5	9	23	53	0.025	2.30	0.45	Good
57	Si wafer	5	9	23	52	0.125	1.93	0.37	Good
58	Si wafer	5	9	21	53	0.150	3.16	0.62	Good
59	Si wafer	5	9	21	53	0.175	2.60	0.51	Good
60	Si wafer	5	9	21	52	0.113	1.54	0.30	Good
61	Si wafer	5	9	21	52	0.200	3.55	0.69	Good
62	Si wafer	5	9	21	84	0.125	1.79	0.35	Good
63	Si wafer	5	9	21	85	0.100	1.85	0.36	Good
64	Si wafer	5	9	21	87	0.113	2.33	0.45	Good
69	Si wafer	5	9	21	1	0.100	1.00	0.20	Good
99	Si wafer	1	6	25	41	0.117	1.00	0.19	Good
100	Si wafer	1	6	25	41	0.055	0.67	0.13	Good
101	Si wafer	1	6	25	41	0.100	0.97	0.19	Good
102	Si wafer	1	6	25	41	0.112	0.50	0.10	Good
103	Si wafer	1	6	25	89	0.117	0.80	0.16	Good
104	Si wafer	1	6	25	89	0.055	0.62	0.13	Good
105	Si wafer	1	6	25	75	0.055	1.25	0.25	Good
106	Si wafer	1	6	25	73	0.100	0.82	0.16	Good
107	Si wafer	1	6	25	72	1.000	0.69	0.14	Good
108	Si wafer	1	6	25	2	0.117	0.81	0.16	Good
109	Si wafer	1	6	25	1	0.055	0.76	0.15	Good
110	Si wafer	1	6	25	1	0.100	0.76	0.15	Good
114	Si wafer	3	6	42	1	0.055	1.14	0.23	Good
115	Si wafer	3	6	42	52	0.055	0.77	0.15	Good
116	Si wafer	3	6	45	52	0.117	1.00	0.20	Good

Sample N°	Substrate	C / mg/mL	pH	T / •C	RH%	S_w / mm/s	T_h / nm	σ / nm	Fit quality
117	Si wafer	3	6	44	52	0.100	0.50	0.10	Good
118	Si wafer	3	6	46	2	0.117	0.69	0.14	Good
119	Si wafer	3	6	44	1	0.100	0.68	0.13	Good
120	Si wafer	3	6	46	82	0.055	0.74	0.14	Good
121	Si wafer	3	6	49	73	0.100	0.72	0.14	Good
122	Si wafer	3	6	47	78	0.117	0.65	0.12	Good
123	Si wafer	3	6	26	48	0.055	0.20	0.04	Good
124	Si wafer	3	6	26	48	0.117	0.21	0.04	Good
126	Si wafer	3	6	25	85	0.055	0.67	0.13	Good
127	Si wafer	3	6	25	84	0.117	0.63	0.15	Good
128	Si wafer	3	6	25	79	0.100	0.88	0.17	Good
130	Si wafer	3	6	25	4	0.117	0.64	0.13	Good
131	Si wafer	3	6	25	4	0.100	0.59	0.11	Good
132	Si wafer	5	6	25	4	0.055	2.00	0.39	Good
133	Si wafer	5	6	25	3	0.117	3.19	0.63	Good
134	Si wafer	5	6	25	0	0.100	2.26	0.45	Good
135	Si wafer	5	6	25	85	0.055	1.91	0.37	Good
136	Si wafer	5	6	24	84	0.117	2.95	0.58	Good
137	Si wafer	5	6	24	83	0.100	2.61	0.51	Good
138	Si wafer	5	6	24	45	0.055	2.21	0.44	Good
139	Si wafer	5	6	24	44	0.117	2.85	0.56	Good
142	Si wafer	5	9	24	43	0.117	1.98	0.39	Good
143	Si wafer	5	9	24	43	0.117	0.79	0.15	Good
145	Si wafer	5	9	26	6	0.100	1.99	0.39	Good
146	Si wafer	5	9	26	73	0.100	4.91	1.00	Average
147	Si wafer	5	9	25	74	0.100	1.21	0.24	Good
148	Si wafer	5	9	25	1	0.100	0.56	0.28	Good
149	Si wafer	5	9	25	1	0.100	1.87	0.36	Good
150	Si wafer	5	9	25	1	0.100	2.00	0.39	Good
151	Si wafer	5	9	25	70	0.100	32.82	8.43	Poor
152	Si wafer	5	9	25	68	0.100	1.00	0.20	Good
153	Si wafer	5	9	25	67	0.100	2.03	0.40	Good
154	Si wafer	5	9	28	66	0.100	1.73	0.34	Good
155	Si wafer	5	6	46	71	0.100	2.62	0.51	Good
156	Si wafer	5	6	46	36	0.100	3.38	0.66	Good
157	Si wafer	5	6	46	1	0.100	3.58	0.71	Good
158	Au	5	6	29	67	0.100	11.24	3.05	Good
159	Si wafer	5	6	29	64	0.100	2.75	0.54	Good
160	Au	5	6	29	64	0.100	12.45	3.53	Good
161	Si wafer	5	6	29	65	0.100	3.38	0.67	Good
162	Au	5	6	29	64	0.100	30.28	6.83	Average/Poor
163	Si wafer	5	6	29	65	0.100	4.35	0.86	Good
164	Au	5	6	29	64	0.100	12.01	4.33	Poor
165	Si wafer	5	6	29	64	0.100	5.07	1.01	Good
166	Au	5	6	44	63	0.100	10.40	3.01	Good/Average

Sample N°	Substrate	C / mg/mL	pH	T / •C	RH%	S_w / mm/s	T_h / nm	σ / nm	Fit quality
167	Si wafer	5	6	44	64	0.100	4.96	0.99	Good
171	Si wafer	3	6	45	66	0.100	1.59	0.32	Good
172	Au	3	6	44	67	0.100	-	-	**-**
173	Si wafer	3	9	32	61	0.100	-	-	**-**
174	Au	3	9	31	61	0.100	2.66	0.52	Good
175	Au	3	9	31	69	0.100	-	-	**-**
176	Si wafer	3	9	31	67	0.100	1.98	0.39	Good
178	Si wafer	5	9	26	50	2.500	39.61	10.08	Poor
179	Si wafer	5	9	26	50	5.000	43.19	10.69	Poor
180	Si wafer	5	9	26	50	7.500	25.47	5.94	Poor
181	Si wafer	5	9	26	49	10.000	9.14	1.92	Poor
182	Si wafer	5	9	26	0	2.500	32.73	8.44	Average
183	Si wafer	5	9	26	0	5.000	42.96	10.66	Average
184	Si wafer	5	9	26	0	7.500	28.96	7.13	Average
185	Si wafer	5	9	26	0	10.000	28.12	6.81	Average
186	Si wafer	5	9	26	67	2.500	1.37	0.28	Good
187	Si wafer	5	9	26	67	5.000	51.42	11.69	Poor
188	Si wafer	5	9	26	68	7.500	33.21	8.54	Poor
189	Si wafer	5	9	26	68	5.000	37.30	9.63	Poor
191	Si wafer	5	6	26	63	5.000	13.95	2.82	Poor
192	Si wafer	5	6	26	63	7.500	5.73	1.24	Poor
193	Si wafer	5	6	26	62	10.000	14.14	2.86	Poor
194	Si wafer	5	6	25	2	2.500	36.90	6.92	Average
195	Si wafer	5	6	25	3	5.000	-	-	Poor
196	Si wafer	5	6	25	0	7.500	54.79	9.98	Poor
197	Si wafer	5	6	40	0	10.000	-	-	Poor
198	Si wafer	5	6	43	2	2.500	11.46	1.92	Average
199	Si wafer	5	6	44	2	5.000	17.05	2.91	Poor
200	Si wafer	5	6	46	2	7.500	26.52	4.91	Poor
201	Si wafer	5	6	46	1	10.000	28.28	5.29	Poor
202	Si wafer	5	6	47	66	2.500	-	-	Poor
203	Si wafer	5	6	48	79	5.000	18.40	3.20	Poor
204	Si wafer	5	6	47	83	7.500	24.27	4.32	Poor

208
209

210 **Table S 4 – Surface roughness calculated from the $h(d)$ profiles (h is the height in *nm* and d is the distance**
211 **in *μm*) for samples corresponding to AFM images in Figure 4 in the main text (Sample list is given in Table**
212 **S 3) and to the bare control silicon substrate in Figure S 5a. For sample 176 in profile Figure 4a) in the main**
213 **text, only the $13 < d$ (μm) < 40 region is considered to avoid the peak and valley artifacts. R_q: root mean**
214 **squared roughness; R_{sk}: skewness; R_v: valley roughness, lowest value of height; R_p: peak roughness, highest**
215 **value of height; Δ_{RpRv}: peak-to-valley roughness, largest height amplitude. In the formulas, n is the number**
216 **of height values in the $h(d)$ profiles.**

Sample N°	R_q / nm	Skewness (R_{sk}) / nm	R_v / nm	R_p / nm	Δ_{RpRv}
	$\sqrt{\dfrac{1}{n}\sum_{i=1}^{n} h_i^2}$	$\dfrac{1}{nR_q^3}\sum_{i=1}^{n} h_i^3$	$\left|\min_i h_i\right|$	$\left|\max_i h_i\right|$	$R_p - R_v$
171	0.58	0.44	-0.87	+1.14	2.01
	0.15	-0.16	-0.39	+0.33	0.72
176	0.19	-0.70	-0.44	+0.28	0.72
	0.10	0.26	-0.35	+0.32	0.67
Control: Si wafer	0.18	0.28	-0.57	+0.74	1.31

217

218   The root mean squared (R_q) roughness lies below 0.60 nm for all samples and practically
219 below 0.2 nm for most of them, including the control. The skewness (R_{sk}), which is indicative
220 of the symmetry of the distribution, shows both slightly positive and negative asymmetry in the
221 height distribution; however, this occurs in a random manner (e.g., positive and negative for
222 the same sample) with R_{sk} being smaller than |0.70| nm and of the same order as for the Si wafer
223 for most samples. The peak-to-valley height, Δ_{RpRv}, between the highest peak (R_p) and lowest
224 valley (R_v) is below 2 nm in the worst case scenario and actually comparable, and even smaller,
225 than the control Si wafer (1.31 nm).

226

227

Figure S 5 – a) AFM image and corresponding height –distance, $h(d)$, profile (white segmeted line) measured on a commercial Si wafer control substrate. b) Large-scale AFM image of the Au control substrate. c) Magnified AFM image of the Au control substrate showing the typical mosaic-like structure composed of Au (111) crystalline domains (white segmented lines). d) IR spectrum measured by AFMIR experiments on the Au substrate. The spectrum is the resul of 15 averaged spectra collected randomly on the corresponding AFM image in b). The gold substrate control displays no IR signal in the IR region between 1900 and 1500 cm⁻¹.

Figure S 6 – a-d) Fluorescence microscopy and e-f) ellipsometry experiments. Sample N° 174 (a) and N° 173 are respectively prepared on gold and Si wafer substrates and they are dip-coated from the same parent solution employing the same conditions. Similarly, sample N° 166 (c,e) and N° 167 (d,f) are respectively prepared on gold and Si wafer substrates and they are dip-coated from the same parent solution employing the same conditions. Exact conditions for each samples are given in Table S 3.

Table S 5 - Fitted values of the thickness, T_h, and fit quality for samples N° 166 and N° 167, respectively prepared using Au and Si wafer substrates from the same G-C18:0 lipid solution and using the same dip-coating parameters (experimental details are in Table S 3). T_h is the average of the thickness values obtained with refractive index of 1.4 an 1.7 (lower and upper maximum reported for homogeneous, dense, lipid bilayers).

Sample N°	Substrate	T_h (RI= 1.4)	T_h (RI= 1.7)	Average T_h	Fit quality
166	Au	12.52	8.27	10.40 ± 3.01	Good
167	Si wafer	5.66	4.26	4.96 ± 0.99	Good

252   If gold and silicon (intended as the native surface oxide layer for the latter) surfaces

253   have comparable dispersive and electron acceptor (acidic) components of the surface energy,

254   respectively in the order of 30 mJ/m^2 and 1 mJ/m^2, the electron donor (basic) component has a

255   sensible difference of several tens of mJ/m^2, a fact which could influence the homogeneity, and

256   even structure, of the G-C18:0 lipid coating between a gold and silicon surface, as shown before

257   for sophorolipid glycolipids.[22] For this reason, the surface homogeneity of the samples dip-

258   coated on a gold substrate is preliminarily probed by ellipsometry and fluorescence microscopy,

259   before the AFMIR analysis. Figure S 6 shows a set of microscopy and ellipsometry data

260   recorded on both silicon and gold substrates dip-coated into the same initial solutions, whereas

261   the modelling strategy of the gold substrates and the fit quality of the corresponding $\Psi(\lambda)$ and

262      $\Delta(\lambda)$ profiles are discussed in the materials and method section and shown in Figure S 3.

263   According to Figure S 6a-d, fluorescence microscopy does not demonstrate a sensible

264   difference in terms of surface distribution of the fluorophore between the lipid-coated gold and

265   silicon substrates: in all cases the images are characterized by a poorly-contrasted,

266   homogeneously-distributed, fluorescence signal. In the case of gold substrates, the signal is

267   superimposed to a mosaic-like structure at scales below 5 μm, and this is due to the typical

268   polydisperse, cellular-like, structure of the surface (111) gold domains, of size between 1 and

269   5 μm, as shown by AFM on the control, lipid-free, gold substrates in Figure S 5b,c. The good

270   matching between the fit and the experimental $\Psi(\lambda)$ and $\Delta(\lambda)$ profiles in the corresponding

271   ellipsometry experiments, Figure S 6e,f, confirm the coating homogeneity on Au- and Si-coated

272   substrates on the cm-scale, although the average thickness seems to be slightly larger (about a

273   factor 2) in the case of a gold substrate (Table S 5). These data show that replacing silicon with

274   gold does not induce major changes in terms of homogeneity of the G-C18:0 lipid coating and

275   for this reason, AFMIR can be reliably employed on lipid-coated gold substrates.

276

277
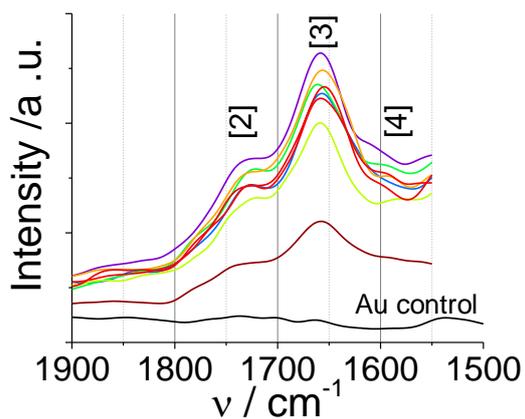
278

279 **Figure S 7 - Non-normalized IR spectra corresponding to the AFMIR experiment performed on G-C18:0**
280 **lipid-coated gold substrates (Sample N°175, Table S 3) dipped at the optimal conditions of S_w= 0.1 mm/s.**
281 **Each spectrum is the average of 5 spectra, randomly collected on the AFM image presented in Figure 5a in**
282 **the main text. The Au control background signal is presented on Figure S 5d and measured on a lipid-free**
283 **gold substrate (Figure S 5b,c).**

284
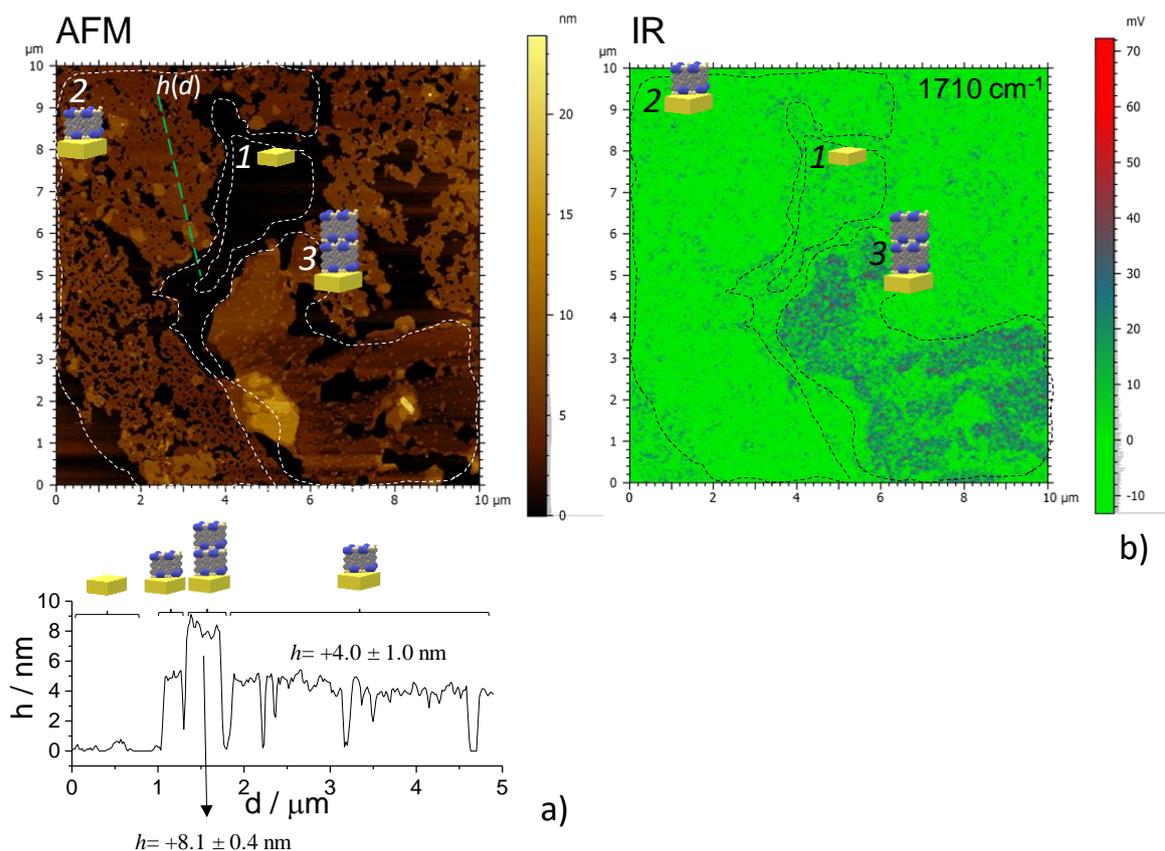
Figure S 8 – Coupled AFMIR experiment performed on sample N° 58 (Table S 3) prepared on a Si wafer substrate. a) AFM image and corresponding thickness profile (green line), $h(d)$, measured along the white thick line. b) 2D IR cartography recorded at 1710 cm^{-1} and corresponding to the AFM image in a). Segmented regions labelled 1, 2 and 3 in a) and b) correspond to the Si wafer substrate (1-labelled), single-layer (2-labelled) and double-layer (3-labelled) G-C18:0 coating.

The 1-labelled region in the AFM image (Figure S 8a) identifies the Si wafer substrate (h= 0 nm), while the 2-labelled region corresponds to a single-layered G-C18:0 coating, of average height over 3 μm, h= +4.0 ± 1.0 nm, as indicated by the $h(d)$ profile in Figure S 8a relative to the continuous white line. The 3-labelled region, on the contrary, shows a brighter coating, corresponding to a doubled lipid layer with an average height, measured over 3 μm, of h= +8.1 ± 0.4 nm ($h(d)$ profile in Figure S 8a). The corresponding 2D IR cartography in Figure S 8b interestingly shows that only a double lipid layer (2-labelled region) provides an IR signal intense enough to be detected. The lack of a signal corresponding to a single layer is explained by a lower amplification of the local electric field due to the use of Si wafer used for this sample instead of gold.

References

304

305 1   K. M. J. Saerens, J. Zhang, L. Saey, I. N. A. Van Bogaert and W. Soetaert, *Yeast*, 2011,
306   **28**, 279–292.

307 2   N. Baccile, M. Selmane, P. Le Griel, S. Prévost, J. Perez, C. V. Stevens, E. Delbeke, S.
308   Zibek, M. Guenther, W. Soetaert, I. N. A. Van Bogaert and S. Roelants, *Langmuir*,
309   2016, **32**, 6343–6359.

310 3   A. I. Novaira, V. Avila, G. G. Montich and C. M. Previtali, *J Photochem Photobiol B*,
311   2001, **60**, 25–31.

312 4   M. Leonard-Latour, R. M. Morelis and P. R. Coulet, *Langmuir*, 1996, **12**, 4797–4802.

313 5   N. Baccile, A.-S. Cuvier, S. Prévost, C. V Stevens, E. Delbeke, J. Berton, W. Soetaert,
314   I. N. A. Van Bogaert and S. Roelants, *Langmuir*, 2016, **32**, 10881–10894.

315 6   H. Fujiwara, *Spectroscopic Ellipsometry: Principles and Applications*, Wiley & Sons
316   Ltd., 2007.

317 7   M. C. Howland, A. W. Szmodis, B. Sanii and A. N. Parikh, *Biophys. J.*, 2007, **92**,
318   1306–17.

319 8   S. Ohki, *J. Theor. Biol.*, 1968, **19**, 97–115.

320 9   T. Fyrner, H. H. Lee, A. Mangone, T. Ekblad, M. E. Pettitt, M. E. Callow, J. A.
321   Callow, S. L. Conlan, R. Mutton, A. S. Clare, P. Konradsson, B. Liedberg and T.
322   Ederth, *Langmuir*, 2011, **27**, 15034–15047.

323 10   C. Valotteau, C. Calers, S. Casale, J. Berton, C. V. Stevens, F. Babonneau, C. M.
324   Pradier, V. Humblot and N. Baccile, *ACS Appl. Mater. Interfaces*, 2015, **7**, 18086–
325   18095.

326 11   R. Arnold, A. Terfort and C. Wöll, *Langmuir*, 2001, **17**, 4980–4989.

327 12   A. S. Duwez, U. Jonas and H. Klein, *ChemPhysChem*, 2003, **4**, 1107–1111.

328 13   R. Luschtinetz, A. F. Oliveira, H. A. Duarte and G. Seifert, *Zeitschrift fur Anorg. und*
329   *Allg. Chemie*, 2010, **636**, 1506–1512.

330 14   Y. T. Tao and M. T. Lee, *Thin Solid Films*, 1994, **244**, 810–814.

331 15   C. Tanford, *The hydrophobic effect: Formation of micelles and biological membranes*,
332   Wiley-Interscience, 1973.

333 16   R. Netrabukkana, K. Lourvanij and G. L. Rorrer, *Ind. Eng. Chem. Res.*, 1996, **35**, 458–
334   464.

335 17   A. Dazzi, R. Prazeres, F. Glotin and J. M. Ortega, *Opt. Lett.*, 2005, **30**, 2388.

336 18   A. Dazzi, F. Glotin and R. Carminati, *J. Appl. Phys.*, 2010, **107**, 1–7.

337 19   J. R. Felts, H. Cho, M. F. Yu, L. A. Bergman, A. F. Vakakis and W. P. King, *Rev. Sci.*

338   *Instrum.*, 2013, **84**.

339   20   A. Centrone, *Annu. Rev. Anal. Chem.*, 2015, **8**, 101–126.

340   21   A. Dazzi and C. B. Prater, *Chem. Rev.*, 2017, **117**, 5146–5173.

341   22   J. Peyre, A. Hamraoui, M. Faustini, V. Humblot and N. Baccile, *Phys. Chem. Chem.*

342   *Phys.*, 2017, **19**, 15227–15238.

343